

Ultrafast laser synthesis of zeolites

Sezin Galioglu^{1*,†}, Mehdi Hagverdiyev^{1*}, Meryem M. Dođan¹, Özgün Yavuz^{2,3}, Ü. Seleme Nizam^{2,3},
Ghaith Makey¹, Aladin Choura^{2,3}, Mesut Laçın^{2,3}, Burcu Akata Kurç⁴, Parviz Elahi⁵, F. Ömer Ilday^{2,3},
Serim Ilday^{2,3,†}

¹ UNAM-National Nanotechnology Research Center & Institute of Materials Science and
Nanotechnology, Bilkent University, Ankara, 06800, Türkiye

² Faculty of Electrical Engineering and Information Technology, Ruhr University Bochum, 44801,
Germany

³ Faculty of Physics and Astronomy, Ruhr University Bochum, 44801, Germany

⁴ Micro and Nanotechnology Programme, Middle East Technical University, 06800, Ankara, Türkiye

⁵ Faculty of Engineering, Özyeđin University, 34794, İstanbul, Türkiye

*The authors have equally contributed to this study.

†To whom correspondence should be addressed: sezin@unam.bilkent.edu.tr & serim.ilday@rub.de

Abstract

Research has demonstrated that zeolite nucleation and growth can be controlled by fine-tuning chemical composition, temperature, and pressure, resulting in structures with diverse porosities and functionalities. Nevertheless, current energy delivery methods lack the finesse required to operate on the femto- and picosecond timescales of silica polymerisation and depolymerisation, limiting their ability to direct synthesis with high precision. To overcome this limitation, we introduce an ultrafast laser synthesis technique capable of delivering energy at these timescales with unprecedented spatiotemporal precision. Unlike conventional or emerging approaches, this method bypasses the need for specific temperature and pressure settings, as nucleation and growth are governed by dynamic phenomena arising from nonlinear light-matter interactions—such as convective flows, cavitation bubbles, plasma formation, and shock waves. These processes can be initiated, paused, and resumed within fractions of a second, effectively “freezing” structures at any stage of self-assembly. Using this approach, we traced the entire nucleation and growth pathway of laser-synthesized TPA-silicate-1 zeolites, from early oligomer formation to fully developed crystals. The unprecedented spatiotemporal control of this technique unlocks new avenues for manipulating reaction pathways and exploring the vast configurational space of zeolites.

1. Introduction

Zeolites are crystalline inorganic materials with well-dispersed and systematically arranged nano and/or micron-sized pores. Their chemical composition, pore dimensions, and high surface area can be tailored to yield diverse functionalities such as selective adsorption and separation, CO₂ capture, host-guest assembly, catalysis, mass transport facilitation, ion exchange, and acting as softeners and gas sensors, which are important in various scientific and industrial applications¹⁻³.

Around 40 zeolitic frameworks are found in nature. Millions of different zeolite frameworks have been

identified computationally, but only 256 were synthesised in the laboratory as recognised by the International Zeolite Association (IZA)⁴. Although new zeolitic frameworks are synthesised regularly, repeatability, stability, and optimisation have been reported as major challenges because the final framework structure and functionalities are sensitive to minor variations in the synthesis parameters⁴⁻⁷. We argue that these problems are related to the energy delivery mechanism and how it drives and controls nucleation and growth.

Heat diffuses gradually into the precursor solution in hydrothermal synthesis processes, creating a spatially varying temperature profile, typically over several hours or days. Nonuniform temperature gradients and reactant concentrations in liquid volume spatially alter the nucleation and growth conditions as more or less favourable. This hinders uniform particle formation and results in a broad crystal size distribution^{8,9}. On the other hand, in microwave synthesis, energy is delivered directly to the reactants, which results in localised heat points throughout the liquid volume. However, lacking an efficient mechanism to dissipate the excess heat, the process creates an unstable, locally superheated liquid, highly sensitive to even minor perturbations, forming low-quality zeolite crystals^{9,10}. Alternatives to these conventional synthesis techniques, such as gamma-ray¹¹, high-energy electron beam irradiation¹², and ultraviolet¹³ radiation, use high-energy radiation to induce ionisation to form hydroxyl free radicals, lowering activation energies and accelerating nucleation and growth. However, complex processes, safety concerns, feasibility issues, and other limitations have hindered their widespread adoption^{11,12}.

The ultrafast laser synthesis approach introduces an entirely different energy delivery mechanism rendering absolute temperature and pressure values less critical. A tiny ultrafast reactor at the focus of a femtosecond laser beam can process a liquid volume of a few thousand μm^3 with extremely high

spatiotemporal energy inputs exceeding 10^6 K/mm at speeds of 300 fs, aligning with the timescales of silica polymerisation and depolymerisation reactions. Nonlinear light absorption (multiphoton) by the precursor solution generates a cascade of events that occur in rapid succession^{14,15}. These include plasma generation, cavitation bubble formation, the emergence of high-speed convective flows^{16,17} and shock (pressure) waves^{18,19}, which facilitate controlled nucleation and growth of nearly uniform zeolite crystals. Using this technique, we synthesised various zeolitic frameworks within a few hours, including MFI, LTA and FAU, with different pore sizes and configurations, and crystallinities surpassing 90% with a wt.% yield of around 70%.

Uniquely, the synthesis can be stopped within fractions of a second by turning off the laser. The laser is electronically controlled and it can be turned on and off within microseconds. This can be repeated as much as needed, allowing for iterative sample collection. Turning off the laser rapidly terminates all the abovementioned emergent phenomena, halting the nucleation and growth. Since no significant residual heat remains in the system to assist further nucleation and growth, the structures formed up to that point are effectively "frozen" in their self-assembled state. Samples can be collected rapidly for nucleation and growth analysis, after which synthesis can be resumed by turning on the laser. Using this capacity, we systematically followed the sequential evolution of the synthesis pathway of TPA-silicate-1 zeolites from the formation of early oligomers to the emergence of fully grown crystals.

2. Results and Discussion

2.1. The energy delivery mechanism

The tiny ultrafast reactor is created by focusing a femtosecond laser beam at the glass-liquid interface (Figures 1a and 1c). This approach mirrors our previous work on quasi-2D colloidal self-assembly^{16,17}, where laser pulses are nonlinearly absorbed through multiphoton absorption (Figure 1b), generating a

cascade of events that drive the self-assembly of a variety of active and passive colloidal particles and living organisms.

Multiphoton absorption of laser pulses by the transparent precursor solution delivers extremely localised energy spatially to a volume of less than $8 \times 10^3 \mu\text{m}^3$ (see Supplementary Document) and temporally with a 300 fs/pulse resolution. As a result, the liquid within the micron-sized reactor reaches temperatures exceeding 10^6 K/mm (see Supplementary Document) but only for a fleeting moment, on the order of femtoseconds. The bulk of the liquid outside the tiny reactor receives no external energy and remains at room temperature. This creates a steep spatiotemporal thermal gradient, and because we focus the beam on the glass-liquid interface, together with the surface tensions (Figure 1c), the thermal gradients facilitate the emergence of convective flows. The flows dissipate excess heat generated in the tiny reactor to the entire liquid volume. This process ensures uniform heating of the entire liquid volume. We measured the average temperature of the precursor solution at various positions during a typical reaction and showed that it saturated at around $90 \text{ }^\circ\text{C}$ (Figure S3 and S4). However, the temperature difference between the bulk liquid ($\sim 90 \text{ }^\circ\text{C}$) and the tiny reactor (10^6 K/mm for 300 fs) is still extremely large. Therefore, steep thermal gradients and all other phenomena are maintained throughout the synthesis.

The intense energy of the femtosecond laser pulses also generates plasma, increasing the concentration of reactive species and promoting nucleation and growth. Plasma formation leads to a sudden rise in pressure. In addition to the spatiotemporal energy localisation, shock waves are triggered, propagating extreme pressures and assisting nucleation and growth. Creating rapid pressure gradients and shock waves helps form cavitation bubbles. These buoyant bubbles and convective flows enhance the efficient mixing of the precursor solution, promoting faster and nearly uniform zeolite synthesis.

Historically, the full potential of ultrafast lasers in zeolite (and other inorganic nanomaterials) synthesis has not been thoroughly explored. Traditional approaches typically involve directing the femtosecond laser at a solid object suspended in liquid to generate plasma to initiate nucleation²⁰. Subsequent hydrothermal synthesis is typically used following the laser treatment to grow the nuclei into mature crystals²¹. We believe that the attempts to process the entire precursor solution in a single step likely faced two major challenges: (1) Insufficient energy deposition to the solution, a challenge compounded by the lack of detailed parameters in existing literature, such as pulse fluence and repetition rate (see our optimisation analysis in Figure 2). (2) The difficulty in initiating nonlinear light-matter interactions necessary for processing the entire liquid volume. This issue, while not always explicitly stated, is suggested by experimental setup diagrams, where the beam is often pointed (which might not be tightly focused) arbitrarily within the bulk liquid, suboptimal for efficient multiphoton absorption.

Moreover, continuous-wave and nanosecond lasers cannot replicate the dynamic conditions that femtosecond lasers achieve. Continuous-wave lasers function more like inefficient furnaces, gradually heating the precursor solution, which only slowly promotes nucleation and growth. Although nanosecond lasers can induce multiphoton absorption, they require significantly higher pulse fluences due to their longer pulse durations and lower peak intensities. This extended pulse duration causes thermal diffusion, leading to heat buildup in the material, which can trigger undesirable thermal effects, such as melting or ablation. This compromises precision, especially in applications requiring spatiotemporal control. In our case, using these lasers could even damage the glass vial.

2.2. The self-assembly mechanism

The initial phase involves triggering silica polymerisation-depolymerisation reactions within the *hot zone* of the laser beam (Figure 1c), effectively serving as a tiny ultrafast reactor for zeolite synthesis. Early-

stage oligomer rings and condensed units, generated with each laser pulse, are systematically dispersed throughout the precursor solution via convective flows and cavitation bubbles. As there is one hot zone and the rest of the liquid is relatively much colder, convective flows continually move between the hot zone and the bulk liquid. This is crucial in continually transporting previously distributed nuclei/particles back to the hot zone, where they grow further during each iteration, evolving into larger structures and maturing into nearly mono-sized and discrete zeolite crystals. This unparalleled efficiency sets ultrafast laser synthesis apart from other methods in the field.

A typical synthesis process captured in Videos 1 and 2 visualises the flow fields at three distinct beam positions: at the glass-liquid interface (left), in close proximity to the interface (middle), and closer to the centre of bulk liquid (right). Velocity field calculations reveal a maximum flow speed of 1190 $\mu\text{m/s}$. Subsequently, an average speed is computed over a smaller time frame to highlight the distinct characteristics of the fields for these beam positions, which appear at the end of Video 2 and are shown in Figure 1d. Significantly, high-speed Marangoni flows manifest exclusively when the beam is focused at the glass-liquid interface, whereas seemingly unstructured slow flows are observed away from the interface. This is expected as surface tensions (Figure 1c) promote the creation of Marangoni flows at the interface^{16,17}, a condition absent at the two beam positions away from the glass walls. Moreover, the transition of the precursor suspension colour from transparent to opaque white in Video 1 signifies the saturation of the liquid volume with fully-grown crystals, which is exclusively achieved when the beam is focused at the interface under the same reaction time.

Mechanical stirring of the precursor solution in conventional hydrothermal synthesis has been explored by employing a gradual rotation of the autoclave, typically within a speed range of 10-20 rpm^{22,23}. This approach has yielded positive results, such as marginally accelerated crystal growth and a relatively

narrow size distribution. We ask if the benefits we report could be explained by the laser-induced convective flows alone. To underscore this point, we deliberately directed the laser beam onto the bulk liquid (avoiding the glass-liquid interface) to prevent the formation of laser-induced high-speed Marangoni flows along with all the dynamic phenomena resulting from multiphoton absorption. We only introduced mechanical mixing to the solution using a magnetic stirrer (Video 3). As expected, no noticeable alteration in colour is discerned within the precursor solution, even after tripling the laser exposure time compared to an equivalent typical laser synthesis reported here.

Moreover, this process can be halted and resumed by turning the laser on and off (Video 4) for rapid cooling and heating of the liquid medium, exerting a profound influence on the kinetics of the chemical reaction. Rapid cooling is possible because laser pulses are the only heat source that acts only for femtoseconds. The excess heat is immediately carried out via convective flows and distributed to the bulk liquid. Without incoming pulses, no significant heat source supports further nucleation and growth (see Supplementary Document). That way, the self-assembled structures up until that point are effectively frozen and preserved. Reintroducing the laser pulses rapidly provides the energy and heat to resume the self-assembly process.

Another great benefit of ultrafast laser synthesis in controlling self-assembly stems from the dynamic control over the rate of energy delivery — a capability absent in both conventional (such as hydrothermal and microwave methods) and recently developed approaches (including assembly-disassembly-organization-reassembly²⁴, seed-directed secondary growth²⁵, ultraviolet¹³, gamma-ray¹¹, and high-energy electron beam irradiation¹²). This is achievable by adjusting pertinent laser parameters such as average laser power, peak power, and pulse energy fluence. For example, we performed a systematic study to determine the optimal conditions for zeolite synthesis by only changing the repetition rate and

pulse fluence (Figure 2 and Table S1). Similar optimisation studies can be readily conducted for various laser parameters to exert control over crystal nucleation and growth for various other zeolitic structures.

2.3. Characteristics of ultrafast laser synthesised zeolites

A selection of laser-synthesised zeolites is shown in Figure 3, with their crystalline identities confirmed via XRD spectroscopy (see also Figure S5 and S6 for MFI-type ZSM-5 and FAU-type Zeolite-Y structures). To ensure the reliability and reproducibility of the synthesised zeolites, we conducted over 120 experiments, consistently yielding similar results (see Figure S7, S8, and S9 for the results of representative experiments).

Our focus centered on TPA-silicalite-1, a well-documented and extensively studied model zeolite. To draw quantitative comparisons, we subjected half of the prepared precursor solution to laser synthesis for 3 hours while the other half underwent a typical hydrothermal synthesis for 48 hours. Comparative analysis of the average crystal size distribution between laser- and hydrothermal-synthesised zeolites reveals distinct outcomes. Laser synthesis yields a narrow distribution with larger crystal sizes (Figures S10a and S10c). In contrast, hydrothermal synthesis results in a broader distribution featuring relatively smaller ones (Figures S10b and S10d). Notably, akin to hydrothermal synthesis, reducing the average crystal size in laser synthesis is feasible by modifying the molar formula's water content from M1 (Figure S10) to M2 (Figure S11) and M3 (Figure S12) (see also Figure S13 and Table S2).

The larger crystal sizes and narrow size distribution of ultrafast laser-synthesised zeolites result from vigorous liquid mixing by the laser-induced convective flows and buoyant cavitation bubbles because it significantly enhances mass transfer and accelerates the movement of reactants within the precursor solution^{26–28}. This promotes faster and more uniform growth conditions for crystals. As explained in the

main section, heat and the reactants diffuse and transport more slowly in conventional hydrothermal synthesis, creating uneven nucleation and growth conditions resulting in larger size variations.

Thermal stabilities, as measured through thermogravimetric (TGA) and differential thermal (DTA) analyses for both laser (Figure S14a) and hydrothermally synthesised (Figure S14b) zeolites, yield comparable outcomes with water removal of 4.2% at around 109 °C in the case of laser and 3.4% at around 76.4 °C in hydrothermal synthesis and removal of 12.1% TPA content for both methods at around 334 °C in the case of laser and 329 °C in hydrothermal synthesis.

Crystallinity and product yield calculations suggest similar results for laser- and hydrothermally synthesised zeolites (Table S2). N₂ adsorption-desorption curves (Figure S15) manifest a Type I isotherm, indicative of a microporous structure²⁹ with the BET surface area of 335.5 m²/g falling within the typical range (332 m²/g - 400 m²/g) observed for laser synthesised TPA-silicalite-1 crystals, which is larger than the hydrothermally synthesised crystals with 275 m²/g surface area³⁰⁻³³. The micropore volume and effective pore size of the laser-synthesised TPA-silicalite-1 crystals are calculated from BET analysis to be 0.164 cm³/g and 5.7 Å, respectively (Figure S16).

2.4. Nucleation and growth pathways

We sampled the process at intervals from the 20th to the 300th minute by turning the laser off and on and identified two distinct regimes for nucleation and growth. Throughout the synthesis, no observable colour change occurred in the precursor solution until the 70th minute. The initially light milky colour at 70th min. transformed to a milky hue by the 90th min., later evolving into an opaque white appearance by the 240th min. (Figure 4a). Subsequent SEM images (Figure 4b) and calculations of average crystal size distribution (Figure 4c) reveal where a high-degree network of smaller crystals with rough surfaces

gradually transitioned into larger, discrete crystals with smoother surfaces. SEM and TEM images of samples collected at the 70th min. suggest that individual crystals are formed by aggregating smaller crystals, each with an average size of ~15 nm. Since those on the surface and contributing to the network by bridging crystal aggregates are electron-beam sensitive, phase-contrast TEM images were performed, revealing a bright appearance and confirming their crystalline nature (Figure 4d).

Moreover, to elucidate the chemical transformations occurring during the formation of these minute crystals, we scrutinised the Si-O-Si and O-Si-O bending and the Si-O-Si symmetric stretching signals using ATR-FTIR spectroscopy. Comparative analysis with molecular dynamics simulations³⁴⁻³⁶ (Figures 5a and 5b) reveals the presence of loosely connected 5-membered ring structures (yellow-filled peak), condensed units of 10T and 22T structures (red-filled peak), and 36T MFI precursors (brown-filled peak) as early as 20th minute of the synthesis. Fully grown MFI structures appear at the 60th minute (grey-filled peak) (see also Figure S17). The evolution of peak relative intensities is tracked until the 300th minute of the reaction. Initially, the signal from early ring vibrations diminishes until the 70th minute and then ceases at the 90th minute, marking the complete consumption of small oligomers. Concurrently, the signal contribution from MFI precursors increases as they assimilate the early oligomers for their self-assembly. After the 70th minute, the signal from fully grown MFI structures increases drastically by consuming the MFI precursors. Accordingly, the signal contribution of the MFI precursors diminished significantly.

We calculated the crystallinity of liquid samples collected at $20 < t < 300$ minutes of the synthesis from XRD data and also from ATR-FTIR analyses (Figure 5c) to correlate them with the self-assembled structures calculated through the molecular dynamics simulations (Figure 5b). Our crystallinity analyses revealed fast and slow sigmoidal growth dynamics for MFI precursor structures and fully-grown crystals, respectively. The consumption of early oligomers by the growing MFI precursor structures until the 90th

min. was much faster than that of MFI precursors by fully-grown zeolite crystals. This is so because strong nonlinear light-matter interactions that drive the nucleation and growth are modified when the precursor solution transitions from transparent to opaque white, affecting the growth rate.

Multiphoton absorption occurs when multiple photons are simultaneously absorbed by the medium, allowing an electron to transition to a higher energy state, even if the energy of each individual photon is insufficient to bridge the gap between energy levels (Figure 1b). This process typically requires high-intensity light, such as our tightly focused ultrafast laser beam, where the photon density is extremely high at the focal point to enable multiple photons to interact with a single atom or molecule in a very short timescale. Multiphoton absorption is strongest when the medium is transparent, so we start our experiments with a transparent precursor solution rather than its gel-like form, typically used in conventional hydrothermal synthesis.

As shown in Figure 4a, the initial transparent solution turns milky white at around 90 minutes, corresponding to where the initial fast growth rate slows in the crystallinity graph in Figure 5c. The slower growth rate eventually plateaus around 240 minutes when the precursor solution is opaque white. However, it is still possible to facilitate multiphoton absorption in an opaque medium if a high-intensity laser beam can create localised regions with enough photons to facilitate this phenomenon. Opaque materials often exhibit nonlinear optical effects (e.g., modified refractive index or absorption coefficient) under the high light intensity provided by an ultrafast laser tightly focused at the focal point. This can promote multiphoton absorption by concentrating light energy in specific regions. This applies to our case, as we observe bubbles, flows, and plasma throughout the synthesis, as seen in Video 1.

2.5. Versatility of the ultrafast laser synthesis technique

Since femtosecond laser pulses provide energy within the relevant timescales of zeolite polymerisation-depolymerisation reactions, it becomes feasible to synthesise zeolites without the customary ageing step. Typically, in zeolite synthesis, the precursor solution undergoes a standard practice of being kept at room temperature for 24 hours post-chemical mixing. To experiment with this, we applied the laser immediately after chemical mixing (without ageing) and successfully synthesised TPA-Silicalite-1 crystals within a few hours (Figure 6a).

An additional distinctive feature of utilising ultrafast lasers is the potential to leverage collective pulse-matter interactions for synthesising diverse topologies and functionalities, thereby further exploring the configurational phase space of zeolites. This is a new interaction regime with different kinetics whereby multiple pulses simultaneously interact with the matter instead of a single pulse. To experiment with this idea, we utilised a home-built ultrafast burst-mode laser³⁷. As shown in Figure 6b, our initial findings with this new light-matter interaction regime produced hierarchical structures with pore openings spanning approximately 20 to 60 nm and 120 to 280 nm, which will be investigated further.

3. Conclusions

The ultrafast laser synthesis technique reported here is a paradigm shift in zeolite synthesis. Femtosecond laser pulses provide extremely localised energy in space and time, allowing high-precision control over energy delivery and reaction kinetics. High spatiotemporal precision prevents unwanted heat accumulation and thermal diffusion, promoting fast synthesis of nearly uniform, high-quality, high-yield crystals. Energy is delivered at timescales compatible with the natural timescales of zeolite polymerisation and depolymerisation reactions, which makes it possible to even eliminate the time-consuming ageing step. The technique opens new possibilities for producing diverse zeolitic structures

and topologies. Various zeolite configurations may be explored by adjusting laser parameters without altering the chemical composition. Additionally, collective light-matter interactions such as the one facilitated by burst-mode lasers can be employed to explore more complex topologies that may be difficult or impossible to achieve using conventional methods, such as millions of computer-generated frameworks. We postulate that the technique cannot be limited to zeolite synthesis as it is not specific to any chemical used in the process. Any other inorganic material synthesis should be possible.

Methods

Experimental Setup

The precursor solution is housed within a glass insert (Supelco, Merck, 0.75 mL), which is encased within a chromatography glass vial (IsoLab, 4 mL, N13) securely positioned using an adjustable sample holder attached to its cap (Figure 1a and Video 1). An ultrafast laser beam (Spectra-Physics, Spirit One, 1040 - 8 - SHG) is directed towards the precursor solution following the optical path outlined in Figure 1a. The laser operates at a central wavelength of 1040 nm, with a pulse duration of 300 fs and a repetition rate of 200 kHz. To generate Figure 2, we either fixed the total deposited energy or pulse energy fluence to investigate the impact of laser parameters on zeolite formation. Consequently, we varied the average laser power from 2.5 W to 5 W and adjusted the repetition rate between 200 kHz and 1 MHz for these experiments.

Video Recordings and Analyses

The experiments were captured using CMOS scientific (DCC1645C-HQ, Thorlabs) and Canon DSLR (Eos) cameras, employing a 10× Nikon objective for imaging. A white light source was positioned on the optical table at an appropriate angle to illuminate the glass vial and enhance visibility. Particle Image Velocimetry (PIV) analyses were conducted on recordings with a frame rate of ~30 fps and a resolution of 1116×891 pixels, utilising DynamicStudio Software from Dantec Dynamics over ~420 frames. Grayscale images of velocity fields were generated for adaptive PIV analyses to calculate the 2D velocity fields on a 2D grid with tiles sized 16×16 pixels. The average displacements in the x - and y -directions were then extracted using the software's MATLAB link option and converted to velocity vectors in units of $\mu\text{m/s}$. These vectors were coloured using a custom MATLAB code in reference 38. These fields were then averaged over time to derive the mean field on the sample within the specified time interval.

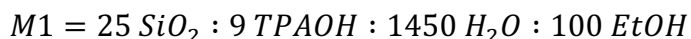
List of Chemicals

We used the following chemicals in zeolite synthesis:

- Aluminium isopropoxide ($\text{Al}(\text{iPro})_3$, > 98%, 220418, Aldrich),
- Al powder (325 mesh, 99.5%, Alfa Aesar),
- Deionized water (DI H_2O , resistivity = 18.2 $\text{M}\Omega$),
- Ethanol (EtOH, 99.99%, IsoLab),
- Sodium hydroxide (NaOH, 99%, Merck),
- Tetraethyl orthosilicate (TEOS, 98%, 131903, Aldrich),
- Tetramethylammonium hydroxide (TMAOH, 25 wt. %, Aldrich),
- Tetrapropylammonium hydroxide (TPAOH, 1M, 254533, Aldrich),
- SiO_2 (Ludox-HS 30, 30 wt. % SiO_2 , pH=9.8, Aldrich), and
- Polystyrene spheres (Micro Particles GmbH, diameter: 250 nm & 500 nm, 2 wt. %).

Synthesis Procedures

Microporous TPA-silicalite-1 zeolite (MFI type): Three different molar formulas^{39,40} were used for MFI-type TPA-Silicalite-1 zeolite synthesis:



We primarily employed the M1 and evaluated the M2 and M3 formulas to demonstrate their potential in reducing average crystal sizes by minimizing water content. To prepare the precursor suspension, 0.25 g of TPAOH was combined with 0.142 g of TEOS in a bottle and stirred at room temperature (RT) for 30 min. Subsequently, 0.512 g of DI water was added to this solution and stirred at RT for 24 h. The same synthesis procedure was applied to the M2 and M3 molar formulas, with 0.07 g of DI water utilised for

M2 and no additional water for M3. Following preparation, the solution was divided into two portions for ultrafast laser and hydrothermal synthesis to compare the resulting zeolite crystals. Hydrothermal syntheses were conducted according to recommended procedures. For batches employing the M1, M2, and M3 molar formulas, hydrothermal syntheses were conducted at 100 °C in an oven (Binder FD 115) for durations of 48 h, 90 °C for 30 h, and 90 °C for 30 h, respectively. Powder products were collected following centrifugation (14000 rpm, Eppendorf Centrifuge 5420), washed with DI water until reaching a neutral pH, and dried overnight at 45 °C in the oven.

Microporous zeolite A (LTA type): $Al(iPro)_3 : 3 TEOS : 7.36 TMAOH : 0.33 NaOH : 192.41 HO_2$ molar formula was used to synthesise microporous zeolite A. 2.17 g of TMAOH was combined with 0.95 g of DI water and stirred for 20 min. Subsequently, 0.17 g of $Al(iPro)_3$ was gradually added to the mixture and stirred for 1 h. After this, 0.53 g of TEOS was introduced to the mixture and stirred for 2 h. Meanwhile, 0.01 g of NaOH and 0.23 g of DI water were mixed in a separate beaker and slowly added dropwise to the main mixture. The resulting blend was stirred for 15 h at RT for ageing. The laser synthesis lasted 2 h, while the hydrothermal reaction was conducted in an oven at 100 °C for 8 h. Powder products were collected using the same procedure as for the TPA-Silicalite-1 zeolites.

Microporous ZSM-5 zeolite (MFI type): $Al(iPro)_3 : 50 TEOS : 9 TPAOH : 9 NaOH : 5709 HO_2$ molar formula⁴¹ was used to synthesise microporous ZSM-5 zeolites. In Solution A, 0.42 g of DI water was combined with 0.26 g of TEOS, followed by the slow addition of 0.005 g of $Al(iPro)_3$. Meanwhile, in a 5 mL beaker, 0.009 g of NaOH powder was dissolved in 1.92 g of DI water and stirred for 2 min. until fully dissolved. This NaOH solution (Solution B) was mixed with 0.23 g of TPAOH. Solution A and Solution B were stirred at RT for 1 h. Subsequently, Solution B was added dropwise to Solution A, stirring the mixture for an additional 24 h at RT for ageing. The laser synthesis lasted 6 h, while the hydrothermal reaction was conducted in an oven at 100 °C for 24 h. Powder products were collected.

Microporous Zeolite Y (FAU type): $9 Na_2O : 0.7 Al_2O_3 : 10 SiO_2 : 160 H_2O$ molar formula⁶ was used to synthesise template-free microporous zeolite Y. Solution A was prepared by dissolving 2 g of NaOH in 4 g of DI water, to which 0.189 g of aluminum powder was gradually added. In Solution B, 10 g of colloidal silica was combined with 1.6 g of NaOH and 3.4 g of DI water to form a turbid suspension. This mixture was then subjected to an oven at 100 °C for 6 min. to convert the turbid suspension into a clear one. Afterwards, Solution A was added drop by drop into Solution B under vigorous stirring, with Solution B cooling down during the mixing process. The resulting clear suspension was left to age 24 h at RT. The laser synthesis procedure lasted 1.5 h, while the hydrothermal reaction occurred in an oven set at 100 °C for 45 h. The powder products were.

Hierarchical ZSM-5 zeolite with a soft template: $Al(iPro)_3 : 50 TEOS : 18 TPAOH : 1.37 CTAB : 171.5 EtOH : 4903 HO_2$ molar formula⁴¹ was used to synthesise hierarchical ZSM-5 zeolites using the soft template cetyltrimethylammonium bromide (CTAB). The primary precursor suspension was aged in an oil bath at 100 °C for 44 h. CTAB, ethanol, and DI water were introduced to the primary precursor suspension. In a separate bottle, a mixture of 1.56 g TEOS and 2.59 g DI water was stirred at RT for 2 h, with 0.03 g of $Al(iPro)_3$ added gradually. Then, 2.76 g of TPAOH was incorporated into the solution, forming Solution A, which was subjected to an oil bath at 40 °C for 2 h. The temperature was subsequently raised to 100 °C to continue stirring the first precursor suspension for an additional 44 h. Meanwhile, 0.075 g of CTAB was dissolved in 8.45 g of DI water in a different bottle and stirred at RT for 15 min. to form Solution B. After 44 h of stirring, Solution B was added to Solution A after cooling to RT. The mixture was stirred in an oil bath at 80 °C for another 2 h. Finally, 1.19 g of ethanol was introduced to the final precursor suspension for further stirring at 80 °C for 2 h. The laser synthesis lasted 5 h, while the hydrothermal reaction occurred in an oven set at 150 °C for 24 h. The powder products

were collected with the additional calcination step at 490 °C for 5 h using Protherm equipment (heating rate = 5 °C/min).

Mesopore-free hierarchical ZSM-5 zeolite: $Al(iPrO)_3 : 50 TEOS : 9 TPAOH : 9 NaOH : 5709 HO_2$ molar formula⁴¹ was used to obtain hierarchical zeolite without using a template to obtain mesopores (*i.e.*, mesoporegens). Solution A was prepared by mixing 0.83 g of DI water with 0.51 g of TEOS, then by gradually adding 0.01 g of $Al(iPrO)_3$. The resulting mixture was stirred at RT for 1 h. Meanwhile, Solution B was prepared concurrently, consisting of 0.018 g of NaOH powder dissolved in 0.96 g of DI water for 2 min. until complete dissolution, followed by adding 0.45 g of TPAOH. Solution B was stirred at RT for 10 min. Subsequently, Solution A was placed in an oil bath at 40 °C, and Solution B was added dropwise while stirring for 3 h at the same temperature. The oil bath temperature was then increased to 100 °C, and the solution was stirred for an additional 44 h. Afterward, the suspension was removed from the oil bath, and 2.88 g of DI water was added to achieve the final precursor suspension. This final solution was stirred at RT for 15 min. The laser synthesis lasted 5 h, while the hydrothermal reaction occurred in an oven set at 150 °C for 24 h. The powder products were collected with the additional calcination step at 490 °C for 5 h using Protherm equipment (heating rate = 5 °C/min).

Hierarchical crystals with a hard template: $M2 = 25 SiO_2 : 9 TPAOH : 480 H_2O : 100 EtOH$ molar formula of MFI-type TPA-Silicalite-1 zeolites were used to synthesize hierarchical crystals. The precursor preparation and ageing steps followed the procedure outlined for TPA-Silicalite-1 zeolite synthesis, with one key variation: the addition of 1.3 mg of 250 nm and 500 nm polystyrene (PS) nanoparticles (Micro Particles GmbH, 2 wt. %) to 500 µl of precursor suspension in separate syntheses. These PS nanoparticles, obtained in powder form, served as hard templates to induce the formation of multi-porous topologies. To achieve the PS in powder form, the PS solution underwent centrifugation (14000 rpm, Eppendorf Centrifuge 5420) followed by overnight drying at 45 °C in an oven. Our synthesis

employed a home-built ultrafast burst mode laser, with each burst (pulse train) lasting 200 ns and a burst repetition rate of 200 kHz. The laser synthesis process lasted 3 h, with the average laser power incident on the glass measured at 3 W. The powder products were collected with the addition of a calcination step performed at 500 °C for 5 h using Protherm equipment (heating rate = 5 °C/min).

Characterisations

The crystallographic structure of the zeolite powder samples was analysed using an X-ray diffraction (XRD) spectrometer (Malvern Panalytical X'Pert Pro Multi-purpose Diffractometer), with a Cu K_{α} X-ray source ($K_{\alpha} = 1.54187 \text{ \AA}$) operating at 45 kV and 40 mA, scanning between the 2θ angle range of 5° - 50°. High-resolution Transmission Electron Microscopy (HR-TEM) images and selected area electron diffraction (SAED) patterns were obtained using a FEI Tecnai G² 20 S Twin microscope operating at 200 kV. Scanning Electron Microscopy (SEM) micrographs were obtained using an FEI Quanta 200F microscope operating at 30 kV after coating the samples with a 10 nm Au/Pd conductive layer using a Gatan 682 Precision Etching Coating system. FEI FP2067/30, equipped with a through-lens detector (TLD) in immersion mode, was used for the Focused Ion Beam Scanning Electron Microscopy (FIB-SEM) micrographs with higher magnifications.

Particle size distribution analyses were conducted using ImageJ and Origin software, based on a minimum of four SEM images of the same sample taken from various locations along the substrate. A fixed number of crystals (298) were utilised for the analyses, with the analysis-statistics toolbox of Origin software employed to generate histograms depicting the average size distribution.

The surface area and pore size distribution of the TPA - Silicalite-1 zeolites were evaluated through Brauer-Emmett-Teller (BET) N₂ adsorption-desorption isotherms at 77.3 K utilising the Quantachrome Autosorb IQ2 MP gas sorption system. A total of 18 synthesis cycles were conducted to obtain the

requisite 150 mg powder sample. Before BET measurements, the powder sample underwent outgassing at 300 °C for 16 h. The BET method facilitated the determination of the total surface area, while the DFT method assessed the micropore volume and the pore size distribution.

Thermal stability, zeolitic water, and structure-directing agent (SDA) content of the TPA - Silicalite-1 zeolites were tested using a thermogravimetric analyses (TGA) spectrometer (SDT650 TGA-DSC) under airflow within 25 °C to 900 °C temperature range with a 5 °C/min. heat flow rate. The Differential Thermal Analysis (DTA) curve is obtained from the TGA data via differentiation using Origin software.

The crystallinity of the products synthesized using M1, M2, and M3 molar formulas was determined using X-ray diffraction (XRD) data from 2 mg powder samples. After subtracting the baseline from the XRD spectrum, the peak areas of the first five significant peaks corresponding to the (501), (051), (151), (303), and (133) planes were calculated and summed within the 22° to 25° 2θ region using Origin software. Following the methodology outlined in the references^{42,43}, we assumed that the crystallinity of the zeolites synthesised via hydrothermal methods represents the maximum achievable crystallinity and serves as the reference value. The crystallinity, denoted as α , was then calculated using the formula below, where PA represents the peak area:

$$\alpha (\%) = \frac{\sum PA_{laser}}{\sum PA_{hydrothermal}} \cdot 100$$

The crystallinity calculations from liquid samples were conducted using Attenuated Total Reflectance Fourier-Transform Infrared (ATR-FTIR) spectroscopy (Bruker Vertex 70 V). Peak deconvolution analyses were performed using a custom MATLAB function⁴⁴. Prior to deconvolution, baseline correction was applied to the FTIR and XRD data using the asymmetric least squares (ALS) algorithm implemented in Origin(Pro) software. We considered the MFI precursor (brown-filled peak) and fully-

grown crystal (grey-filled peak) to calculate the IR crystallinity index. To calculate the XRD crystallinity, we instead considered the total area under all 5 peaks. The sums were then normalised to [0,1] range.

The 4-parameter logistic function was used to fit the crystallinity indices given by

$$f(x) = d + \frac{a - d}{1 + \left(\frac{x}{c}\right)^b}$$

where x denotes the time.

The product yield (wt.%) was determined by dividing the weight of the powder product by the weight of SiO₂ in the batch suspension. The measurement of the powder product was conducted post-centrifugation and drying. The calculated water and TPA contents obtained from TGA-DTA were deducted from the total mass. The batch SiO₂ weight was computed based on the molar formula.

References

1. Y. Li, J. Yu, *Nat Rev Mater* **2021**, *6*, 1156.
2. R. L. Siegelman, E. J. Kim, J. R. Long, *Nat Mater* **2021**, *20*, 1060.
3. E. T. C. Vogt, B. M. Weckhuysen, *Chem Soc Rev* **2015**, *44*, 7342.
4. C. S. Cundy, P. A. Cox, *Chem Rev* **2003**, *103*, 663.
5. W. Chaikittisilp, T. Okubo, *Science* **2021**, *374*, 257.
6. H. Awala, J. Gilson, R. Retoux, P. Boullay, J. Goupil, V. Valtchev, S. Mintova, **2015**, *14*, 447.
7. E. Ng, D. Chateigner, T. Bein, V. Valtchev, S. Mintova, *Science* **2012**, *335*, 70.
8. Z. Liu, J. Zhu, T. Wakihara, T. Okubo, *Inorg Chem Front* **2019**, *6*, 14.
9. M. Nüchter, B. Ondruschka, W. Bonrath, A. Gum, *Green Chemistry* **2004**, *6*, 128.
10. G. A. Tompsett, W. C. Conner, K. S. Yngvesson, *ChemPhysChem* **2006**, *7*, 296.
11. X. Chen, M. Qiu, S. Li, C. Yang, L. Shi, S. Zhou, G. Yu, L. Ge, X. Yu, Z. Liu, N. Sun, K. Zhang, H. Wang, M. Wang, L. Zhong, Y. Sun, *Angewandte Chemie - International Edition* **2020**, *59*, 11325.
12. J. Chen, M. Zhang, J. Shu, M. Yuan, W. Yan, P. Bai, L. He, N. Shen, S. Gong, D. Zhang, J. Li, J. Hu, R. Li, G. Wu, Z. Chai, J. Yu, S. Wang, *Angewandte Chemie - International Edition* **2021**, *60*, 14858.
13. G. Feng, P. Cheng, W. Yan, M. Borona, X. Li, J. H. Su, J. Wang, Y. Li, A. Corma, R. Xu, J. Yu, *Science* **2016**, *351*, 1188.
14. J. P. Longtint, C.-L. Tien, *Int. J. Heat Mass Transfer* **1997**, *40*, 951.
15. J. Noack, A. Vogel, *IEEE Journal of Quantum Electronics* **1999** *35*, 1156.
16. S. Ilday, G. Makey, G. B. Akguc, Ö. Yavuz, O. Tokel, I. Pavlov, O. Gülseren, F. Ömer Ilday, *Nat Commun* **2017**, *8*.
17. G. Makey, S. Galioglu, R. Ghaffari, E. D. Engin, G. Yıldırım, Ö. Yavuz, O. Bektaş, S. Nizam, Ö. Akbulut, Ö. Şahin, K. Güngör, D. Dede, H. V. Demir, F. Ö. Ilday, S. Ilday, *Nat Phys* **2020**, *16*, 795.
18. K. Eidmann, J. Meyer-Ter-Vehn, T. Schlegel, S. Hü, *Phys Rev E* **2000**, *62*, 1202.
19. A. L. Gaeta, *Phys Rev Lett* **2000**, *84*, 3582.
20. L. Franzel, M. F. Bertino, Z. J. Huba, E. E. Carpenter, *Appl Surf Sci* **2012**, *261*, 332.
21. M. Navarro, Ú. Mayoral, E. Mateo, R. Lahoz, G. F. De La Fuente, J. Coronas, *ChemPhysChem* **2012**, *13*, 736.

22. X. Li, Z. Wang, J. Zheng, S. Shao, Y. Wang, Y. Yan, *Chinese Journal of Catalysis* **2011**, 32, 217.
23. Q. Ge, J. Shao, Z. Wang, Y. Yan, *Microporous and Mesoporous Materials* **2012**, 151, 303.
24. M. Mazur, P. S. Wheatley, M. Navarro, W. J. Roth, M. Položij, A. Mayoral, P. Eliášová, P. Nachtigall, J. Čejka, R. E. Morris, *Nat Chem* **2016**, 8, 58.
25. H. Dai, Y. Shen, T. Yang, C. Lee, D. Fu, A. Agarwal, T. T. Le, M. Tsapatsis, J. C. Palmer, B. M. Weckhuysen, P. J. Dauenhauer, X. Zou, J. D. Rimer, *Nat Mater* **2020**, 19, 1074.
26. F. Rosenberger, *Fundamentals of Crystal Growth I*, Springer-Verlag, New York, **1979**.
27. Y. Niu, S. Du, L. Sheng, W. Xiao, X. Jiang, G. He, *Green Chemical Engineering* **2021**, 2, 57.
28. A. K. Pandey, H. Upreti, in *Advances in Mathematical and Computational Modeling of Engineering Systems*, CRC Press, **2023**, pp. 295–314.
29. M. Thommes, K. Kaneko, A. V. Neimark, J. P. Olivier, F. Rodriguez-Reinoso, J. Rouquerol, K. S. W. Sing, *Pure and Applied Chemistry* **2015**, 87, 1051.
30. W. Corkery, B. W. Ninham, *Zeolites* **1997**, 18, 379.
31. M. Tawalbeh, F. H. Tezel, B. Kruczek, S. Letaief, C. Detellier, *Journal of Porous Materials* **2013**, 20, 1407.
32. M. Razavian, S. Fatemi, M. Masoudi-Nejad, *Adsorption Science & Technology* **2014**, 32, 73.
33. L. Tosheva, B. Mihailova, V. Valtchev, J. Sterte, *Microporous and Mesoporous Materials* **2000**, 39, 91.
34. D. Lesthaeghe, P. Vansteenkiste, T. Verstraelen, A. Ghysels, C. E. A. Kirschhock, J. A. Martens, V. Van Speybroeck, M. Waroquier, *Journal of Physical Chemistry C* **2008**, 112, 9186.
35. C. Y. Hsu, A. S. T. Chiang, R. Selvin, R. W. Thompson, *Journal of Physical Chemistry B* **2005**, 109, 18804.
36. C. E. A. Kirschhock, R. Ravishankar, F. Verspeurt, P. J. Grobet, P. A. Jacobs, J. A. Martens, *Journal of Physical Chemistry B* **1999**, 103, 4965.
37. P. Elahi, C. Kerse, H. Hoogland, Ö. Akçaalan, D. K. Kesim, B. Çetin, R. Holzwarth, F. Ö. Ilday, B. Öktem, M. D. Aşık, S. Yavaş, H. Kalaycıoğlu, *Nature* **2016**, 537, 84.
38. J. Q. Krimmer, “Quiver magnitude dependent color in 2D and 3D, MATLAB Central File Exchange,” **2023**.
39. J. Hedlund, S. Mintova, J. Sterte, *Microporous and Mesoporous Materials* **1999**, 28, 185.

40. B. J. Schoeman, J. Sterte, J. E. Otterstedt, *Stud Surf Sci Catal* **1994**, 83, 49.
41. Y. Zhu, Z. Hua, Y. Song, W. Wu, X. Zhou, J. Zhou, J. Shi, *J Catal* **2013**, 299, 20.
42. J. Qi, T. Zhao, X. Xu, F. Li, G. Sun, *Journal of Porous Materials* **2011**, 18, 509.
43. K. Jiao, X. Xu, Z. Lv, J. Song, M. He, H. Gies, *Microporous and Mesoporous Materials* **2016**, 225, 98.
44. T. O'Haver, "MATLAB Central File Exchange" can be found under <https://www.mathworks.com/matlabcentral/fileexchange/23452-ipf-arg1-arg2-arg3-arg4>, **2024**.

Figure Captions

Figure 1. (a) The sketch of the experimental setup shows a half-wave plate (HWP) and a polarizing beam splitter (PBS) placed after the laser to adjust the average power incident on the precursor suspension. A lens focuses the beam to induce fluid flows to start the reaction. (b) A simplified sketch depicts linear and nonlinear absorption processes. 1PA, 2PA, and MPA indicate the absorption of one, two, and multiple photons. (c) Schematics illustrating the working mechanism of a tiny ultrafast reactor at the glass-liquid interface. Reactions are initiated in the *hot zone* near the beam waist (W_0), which is twice the Rayleigh length (Z_R), the distance along the beam's propagation direction from the waist to the position where the cross-section area is doubled (*i.e.*, the beam radius is increased by a factor $\sqrt{2}$). (d) Average flow fields calculated from the video recordings where the beam was focused at the glass-liquid interface (left), close to the interface (middle), and within the bulk liquid (right) (insets are images captured from video recordings).

Figure 2. Graph depicting the optimal laser parameters for zeolite formation: The repetition rate increases while maintaining the total deposited energy and pulse fluence constant (T1, T2, T3, T4). Pulse fluence is halved while keeping the total deposited energy and repetition rate unchanged (T5). Pulse fluence is doubled while maintaining the total deposited energy and repetition rate constant (T6). The crystallinity (C) and weight percentage yield (Y) values are provided under each trial to characterise ultrafast laser-synthesised zeolites.

Figure 3. Scanning (left) and Transmission (middle) Electron Microscopy (SEM and TEM) images of (a) TPA-Silicalite-1, (b) Zeolite A, (c) hierarchical ZSM-5 with a soft template, and (d) mesoporogen-free hierarchical ZSM-5 zeolites. The left panel insets show unit cell structures (lower left) and SEM images of individual crystals (upper right). The middle panel insets show Selected Area Diffraction

(SAD) patterns. X-Ray diffraction spectrums of the laser- (blue, upper) and hydrothermal-synthesised (red, middle) zeolites are compared to their IZA references (black, lower layer) at the rightmost panel.

Figure 4. (a) Photographs taken at different stages of laser synthesis show colour change from transparent to milky white and opaque white as the reaction time increases. (b) SEM images show the evolution of crystals from rough to smoother surfaces as the reaction time increases. (c) Average crystal size distribution plots for zeolites synthesised in various reaction times. (d) TEM images of crystals obtained after 70th minute of reaction time show rough surface contours (dashed red ellipses). The phase contrast TEM images show that these marked regions appear bright, confirming their crystalline nature.

Figure 5. (a) Molecular dynamics simulations show the IR band shift corresponding to different nucleation and growth stages of silicalite-1 zeolites. The image is reproduced from Figure 4 of reference [34]. (b) The IR spectrum of zeolites with signal contributions from loosely connected 5-membered ring structures (yellow-filled peak centered at $\sim 650\text{ cm}^{-1}$) to condensed units of 10T and 22T structures (red-filled peak centered at $\sim 600\text{ cm}^{-1}$), 36T MFI precursors (brown-filled peak centered at $\sim 560\text{ cm}^{-1}$), and fully grown MFI structures (grey-filled peak centered at $\sim 540\text{ cm}^{-1}$). (c) The graph shows the sigmoidal growth of the crystallinity index calculated from ATR-FTIR (red triangles) and XRD (blue squares) to synthesis time. MFI precursor and matured crystal growth are considered for the fading red (until the 90th minute) and blue (after the 90th minute) regions, respectively.

Figure 6. (a) SEM image (upper) and XRD pattern (lower) illustrating laser-synthesised TPA-Silicalite-1 without the preliminary ageing step (exempting the 24-hour stirring of the precursor suspension at room temperature). (b) SEM and TEM images showcase laser-synthesised hierarchical structures.

Video Captions

Video 1. Video recording of an experiment showing colour change of the precursor solution from transparent to opaque white.

Video 2. Video recordings (2nd row) and vector field analyses of the flows (3rd row) for three experiments (1st row), where the laser beam is focused on the glass-liquid interface (left), a position close to the interface (middle), and closer to the centre of bulk liquid (right).

Video 3. Video recording of the experiment where laser beam position does not support multiphoton absorption and the emergence of related dynamic phenomena. Instead, the solution is mixed by external mechanical stirring using a magnetic stirrer.

Video 4. Video recording of the experiment where the laser synthesis is halted and resumed multiple times.

Acknowledgements: This work was supported by European Research Council (ERC) under the European Union’s Horizon 2020 research and innovation programme (grant agreements 853387 and 617521) and TUBITAK under projects 118F115, 120F147, and 123F473. The authors thank Dr. Paul Reppen for valuable discussions and Mete Duman for his assistance in drawing Figure 1a. **Author contributions:** S.G. and S.I. designed the research. S.G., M.H., and M.M.D. performed the experiments and characterisations. S.G., M.H., M.M.D., Ü.S.N. and S.I. analysed the data. F.Ö.I., Ö.Y., G.M., M.L., and A.C. helped design the experimental setup and discussed the results. Ö.Y. provided the energy calculations. B.A.K. provided facility access for some critical instruments and helped with those experiments. P.A. built the home-built ultrafast burst-mode laser. S.I. wrote the paper. All authors read and discussed the final manuscript. **Competing interests:** The authors declare that they have no competing interests. **Data, code, and materials availability:** All data needed to evaluate the conclusions in the paper are present in the paper and/or the supplementary materials. Additional data, code, or material related to this paper may be requested from the corresponding author.

Supplementary Information

Supplementary text

Figures S1 to S17

Tables S1 to S3

Figure 1

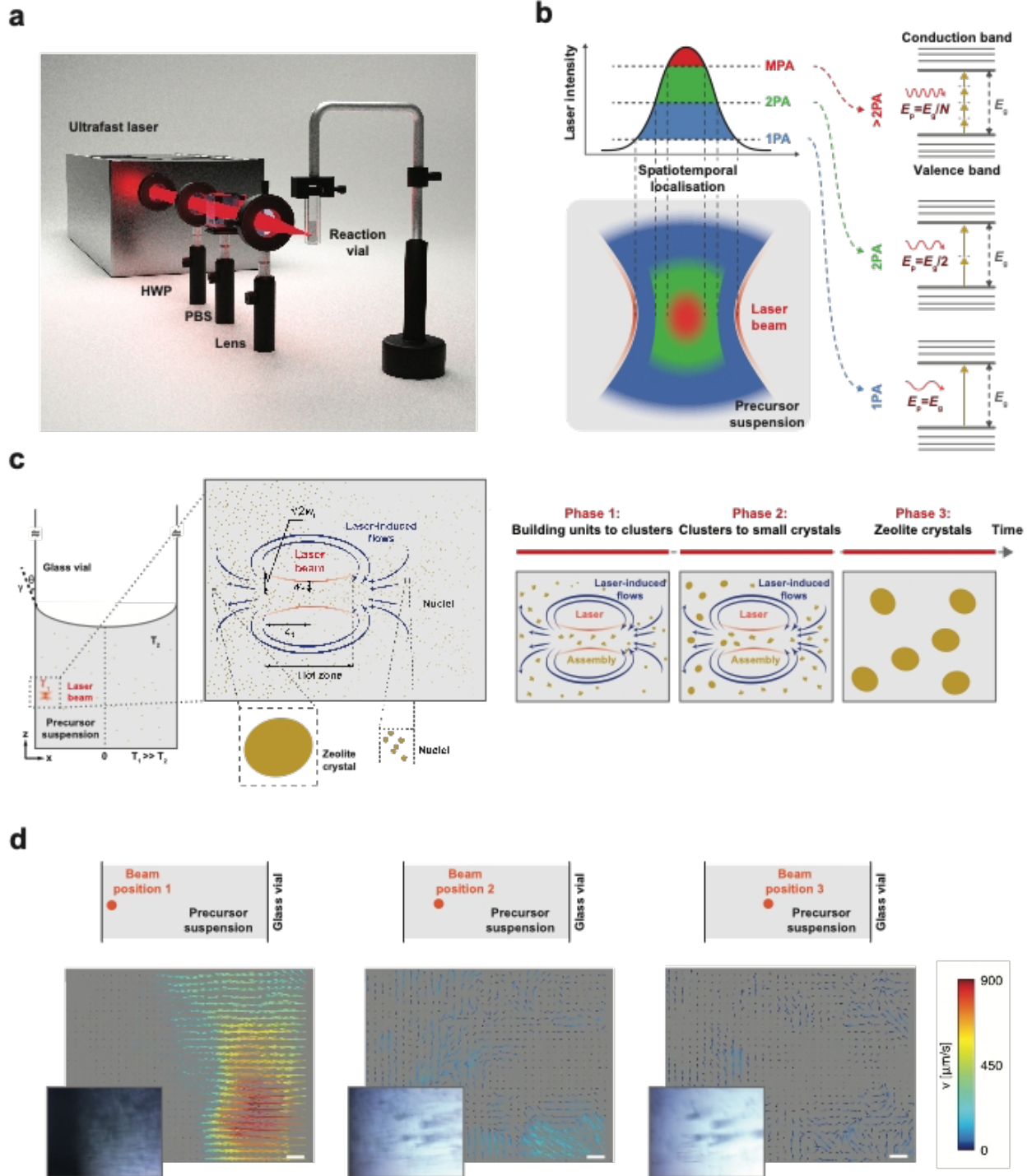


Figure 2

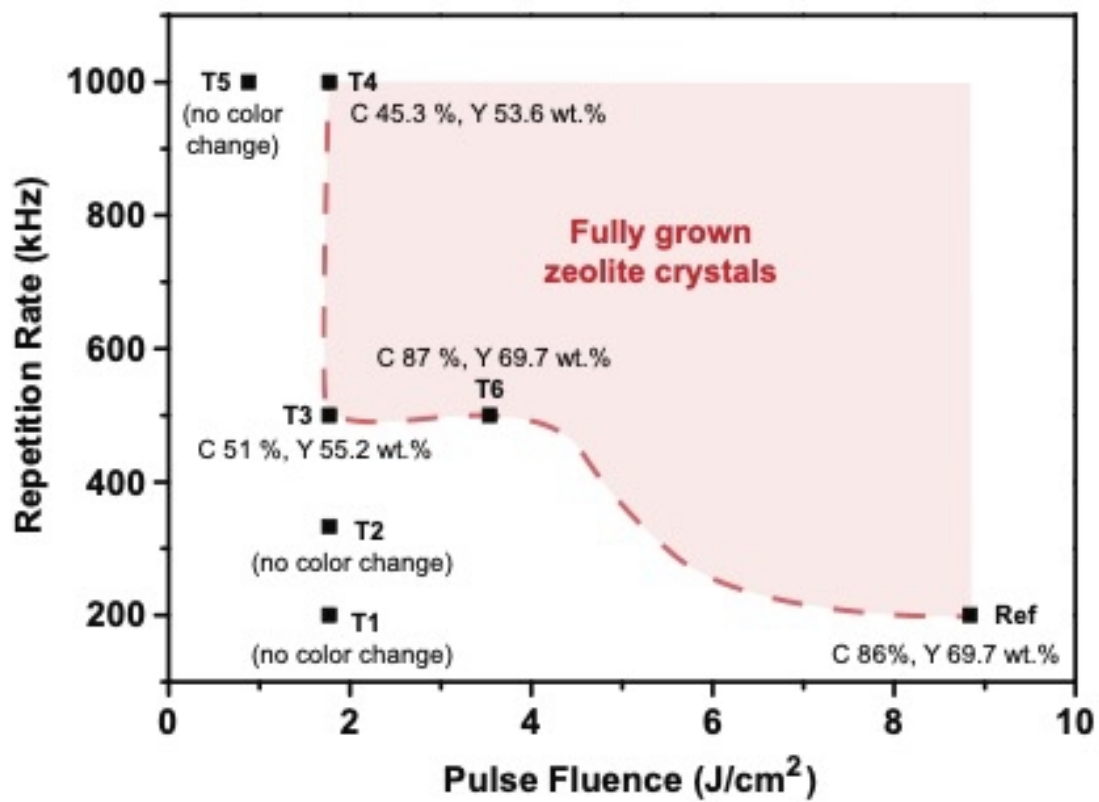


Figure 3

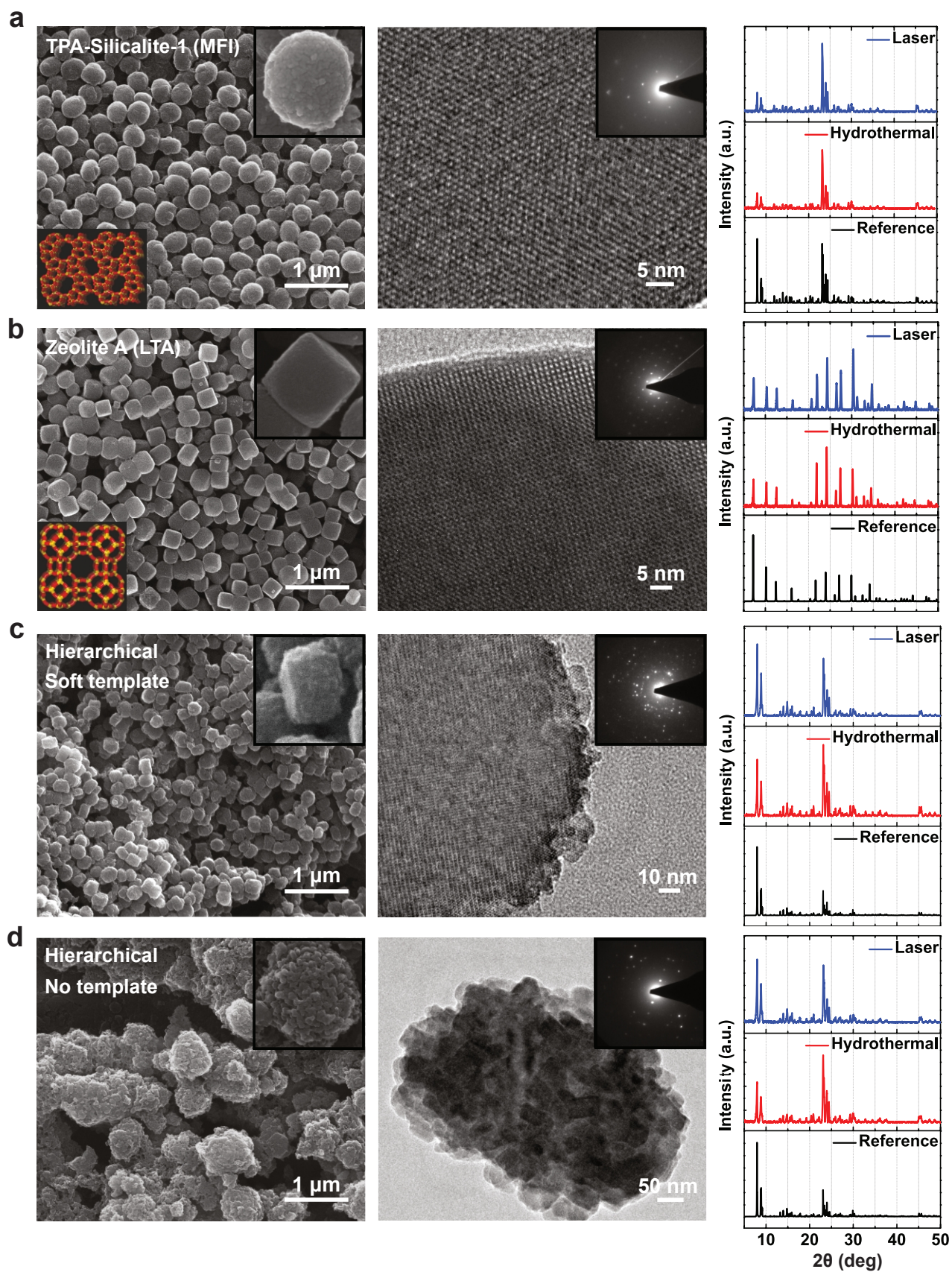


Figure 4

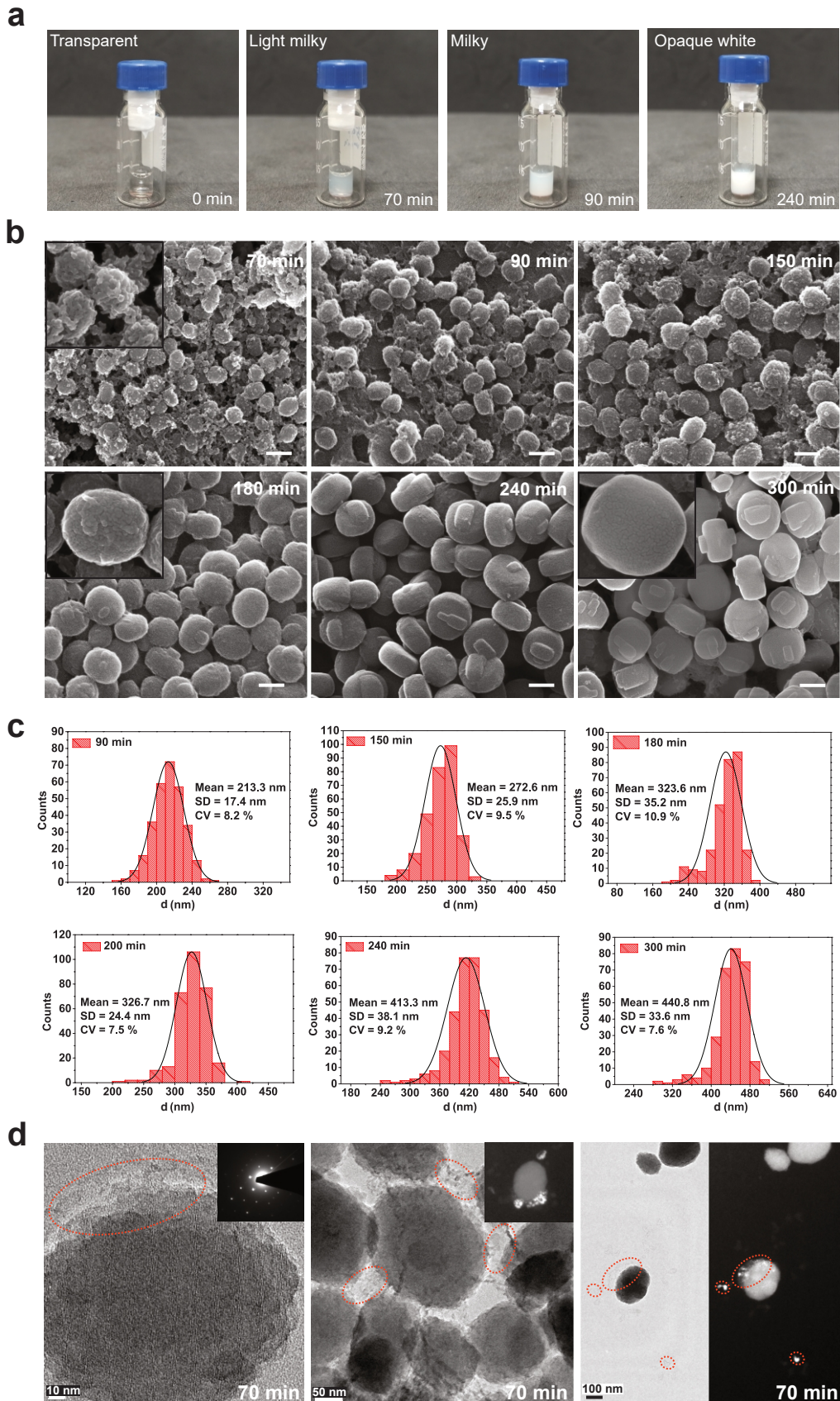


Figure 5

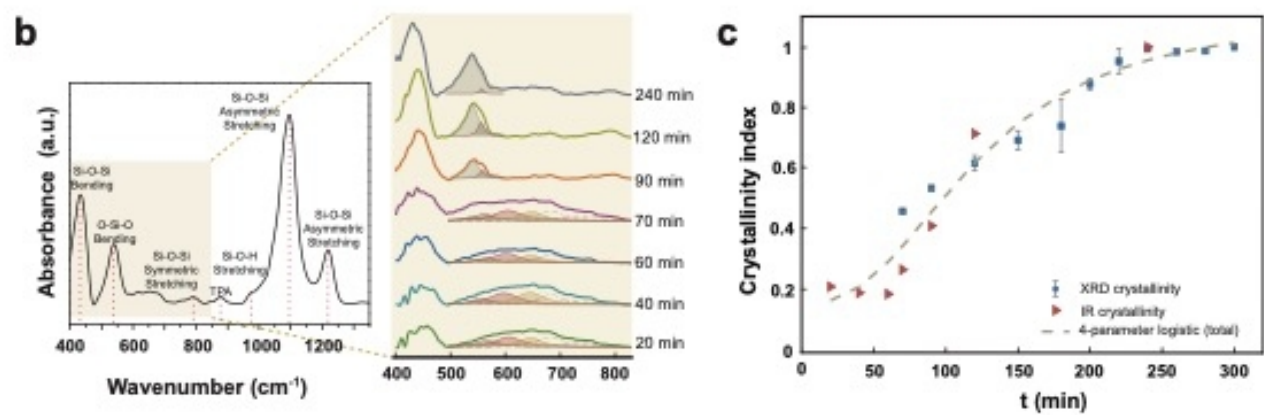
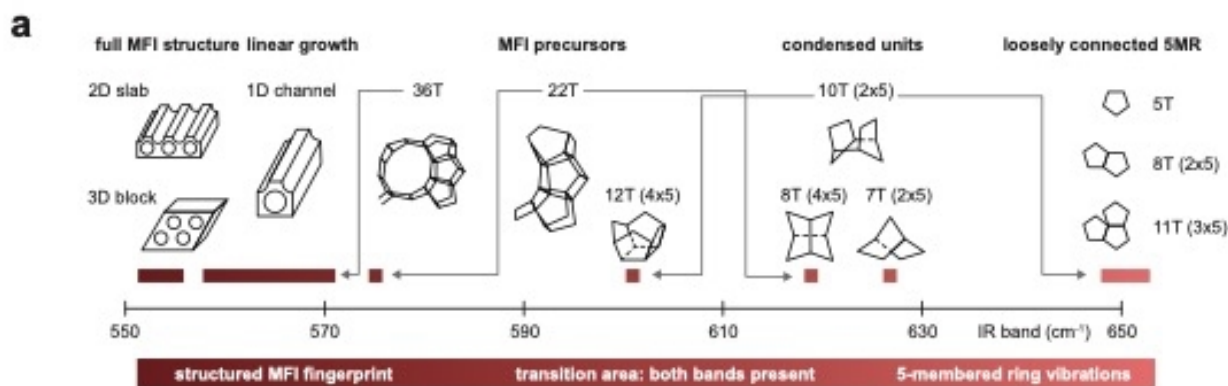
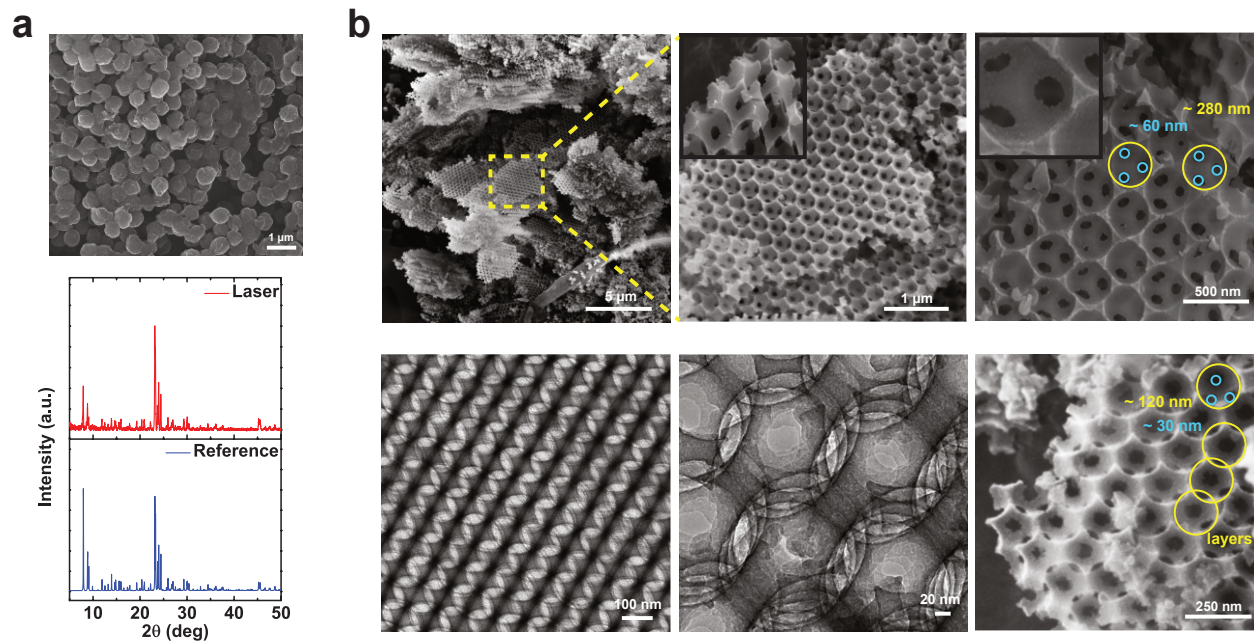


Figure 6



Supplementary Document

Ultrafast laser synthesis of zeolites

Sezin Galioglu^{1*,†}, Mehdi Hagverdiyev^{1*}, Meryem M. Dođan¹, Özgün Yavuz^{2,3}, Ü. Seleme Nizam^{2,3},
Ghaith Makey¹, Aladin Choura^{2,3}, Mesut Laçın^{2,3}, Burcu Akata Kurç⁴, Parviz Elahi⁵, F. Ömer Ilday^{2,3},
Serim Ilday^{2,3,†}

¹ UNAM-National Nanotechnology Research Center & Institute of Materials Science and
Nanotechnology, Bilkent University, Ankara, 06800, Türkiye

² Faculty of Electrical Engineering and Information Technology, Ruhr University Bochum, 44801,
Germany

³ Faculty of Physics and Astronomy, Ruhr University Bochum, 44801, Germany

⁴ Micro and Nanotechnology Programme, Middle East Technical University, 06800, Ankara, Türkiye

⁵ Faculty of Engineering, Özyeđin University, 34794, İstanbul, Türkiye

*The authors have equally contributed to this study.

†To whom correspondence should be addressed: sezin@unam.bilkent.edu.tr & serim.ilday@rub.de

Estimation of the energy absorption

The power losses were measured due to light passing through different interfaces and mediums (Figure S1), where the glass insert and vial wall thicknesses were measured as 0.92 mm and 1.16 mm.

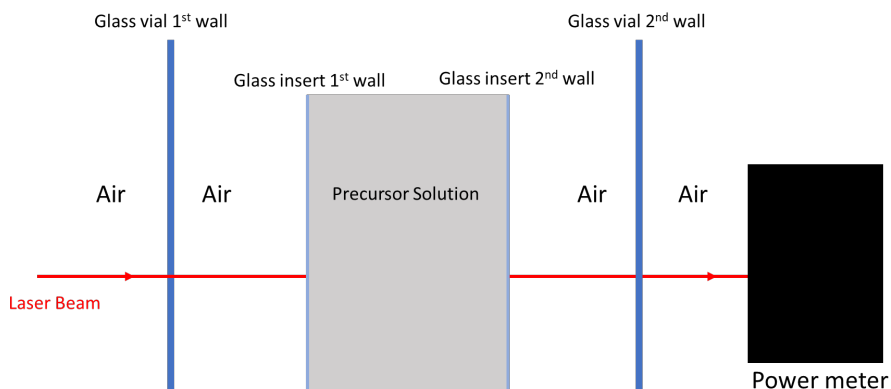


Figure S1. Schematic showing main optical loss mechanisms due to multiple interfaces and mediums.

Figure S2 shows the interfaces where we measured light transmittance from the air – glass vial – air (T_1 and T_2), air – glass insert – air (T_3 and T_4), and glass insert – precursor solution – glass insert (T_5 and T_6) interfaces. We calculated T_1 and T_2 by measuring the light passing through an empty glass vial. Similarly, T_3 and T_4 were measured using an empty glass insert.

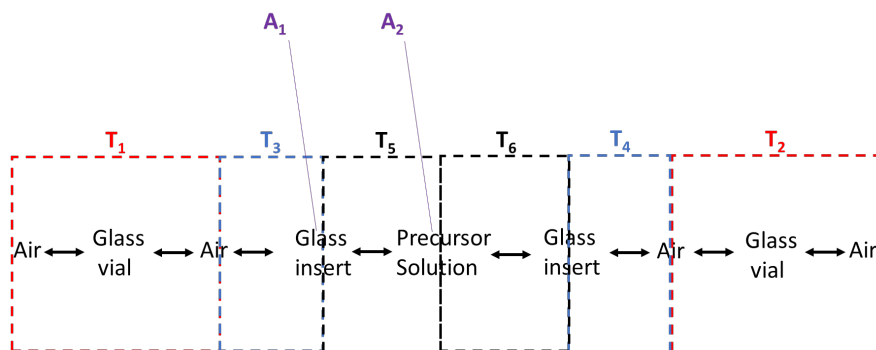


Figure S2. Schematic showing the type of measurements taken at each interface.

Next, the light absorbance by the 1st wall of the glass insert (A_1) and the precursor solution (A_2) was measured by filling the glass insert with precursor solution. During absorbance measurements, recorded average power values fluctuated due to the formation of plasma, fluid flows, and bubbles; therefore, we calculated the average value. Furthermore, we assumed that the refractive index of the precursor solution was similar to that of the water and calculated that the precursor solution absorbs only 22.5% of the incoming average laser power.

The interaction volume (V_i) was calculated using the Rayleigh length (Z_R) and beam waist (b) as below. The beam spot size was measured to be $9 \mu m$ using a beam profiler (Thorlabs).

$$Z_R = \frac{\pi \omega_0^2}{\lambda}$$

$$Z_R = \frac{(3.14)(4.5 \times 10^{-6})^2}{(1040 \times 10^{-9})}$$

$$Z_R = 61.1 \mu m$$

$$b = 2 Z_R = 122.2 \mu m$$

$$V_i = \pi \omega_0^2 b$$

$$V_i = (3.14)(4.5 \mu m)^2(122.2 \mu m)$$

$$V_i = 7.77 \cdot 10^{-6} mm^3$$

The molarity of this volume was calculated assuming the homogenous distribution of SiO_2 to the interaction volume by the flows. The pulse energy can be calculated by dividing the average laser power by the repetition rate, and from here, the energy deposited to the interaction volume can also be calculated. However, it should be noted that these calculations are just estimates based on the assumptions discussed above. Various energy dissipation mechanisms (mainly the plasma, bubble, and flow formations) are also ignored (see explanations below). Therefore, our estimations can only be used to compare the experimental results shown in Figure 2.

Calculation of the thermal gradients

Determining the absorbed energy by the precursor solution is exceedingly challenging due to several factors, primarily the complex optical properties of the solution's constituents, especially their nonlinear characteristics. Convective flows, plasma, and cavitation bubbles also introduce dissipative and scattering effects. The bubbles, varying in size, are difficult to accurately monitor due to imaging and tracking challenges, and their migration due to buoyancy forces complicates matters further. The interaction between flows and bubbles leads to light scattering, while plasma formation significantly alters absorption dynamics. Moreover, linear losses occur due to multiple reflections of light from the glass walls. Our estimates suggest that the solution absorbs less than a quarter of the incident power, even considering only linear losses.

The temperature gradient is calculated by considering the energy transfer from laser pulses to the sample solution, excluding the abovementioned complexities. To simplify, we made several assumptions for a rough estimate. First, we considered the sample solution to be pure water, ignoring the absorption caused by solvents. Second, we assumed the laser absorption to be purely linear. Finally, we considered diffusion to be the dominant heat transfer mechanism. These simplifications provide a lower bound for the temperature gradient because (a) impurities in the water, especially carbon-based ones, would increase the absorption rate, and (b) including nonlinear effects would further enhance absorption. Thus, the actual thermal gradients are expected to be much greater than this estimation.

In our calculations, we used the experimental laser parameters as repetition rate $f_R = 200$ kHz and average incident power to the sample $P_{\text{avg,inc}} = 6$ W. As we calculated above, only 22.5% of the laser power is absorbed by the solution; therefore the absorbed average power is $P_{\text{avg,ab}} = 1.35$ W, and the energy absorbed per pulse is $E_{\text{pulse,ab}} = P_{\text{avg,ab}} f_R^{-1} = 6.75$ μJ . The temperature rise due to a pulse can be calculated as:

$$\Delta T = \frac{Q}{mC}$$

where Q is heat energy, heat-affected area, and $C = 4.18$ J/(g°C) is the specific heat, $m = 7.77$ ng is the water mass within the interaction area (cylinder around the focal point of the laser beam). Assuming all the energy absorbed from a laser pulse is converted to heat, the temperature increment per pulse can be calculated as $\Delta T = 20.8$ °C.

Having a pulse absorbed by the solution, there is a time gap for the next pulse, which is 5 μs precisely for $f_R = 200$ kHz. During this time, the hot water can be carried away from the affected area by convective flows and diffusion. Between the two consecutive pulses, the displacement would only be 6 nm. In other words, it takes ~ 100 ms to replenish the heat-affected volume totally, which is five orders of magnitude higher than the time between the arrival of the pulses.

The diffusion coefficient of the water is considered to be $D = 0.143$ mm²/s. The time that needs to be spent for the temperature of the heat-affected area to reduce to half can be calculated as $\Delta t = 444$ μs , which is two orders of magnitude higher than the separation between pulses. Therefore, we can safely assume that the heat accumulation scales linearly with the number of pulses. With a laser having a repetition rate of $f_R = 200$ kHz, it takes approximately 1 second to reach a temperature gradient of 10^6 K/mm.

Temperature profiling of the suspension

The suspension temperature was measured using a thermocouple probe during a typical synthesis. The thermocouple was coupled to a multimeter connected to a computer to record the measurements for 20 minutes (Figure S3). The laser beam was blocked within the first 2 minutes, and then the temperature increased sharply to ~ 95 °C and stabilised.

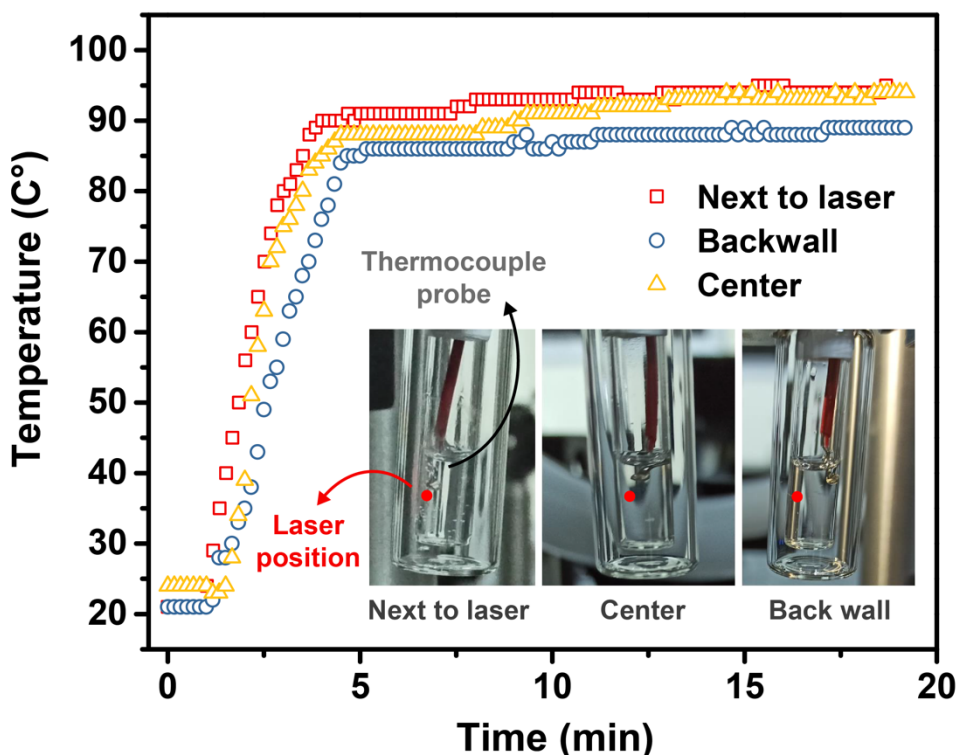


Figure S3. Recorded temperature readings with the thermocouple positioned at the front wall near the beam (position 1), center of the bulk liquid (position 2), and back wall away from the beam (position 3).

The energy delivery by ultrafast lasers is spatially and temporally "localised." Upon the arrival of a pulse, the local temperature rises almost instantaneously (within femtoseconds), corresponding to extremely high thermal gradients. However, this rise is limited to the duration of the pulse, and the temperature begins to cool right away until the next pulse arrives within one or few microseconds. Basically, the local temperature is driven periodically, momentarily rising to very high values that greatly speed up the chemical reaction, but for the briefest duration. The steady-state or time-averaged (over multiple pulse periods, *i.e.*, microseconds) value of the local temperature does not need to be high, at around 90 C. This is a beautiful aspect of ultrafast pulses, efficiently driving chemical processes without loading much thermal energy to the target. We can clarify this with a cartoon-like drawing, as shown in Figure S4.

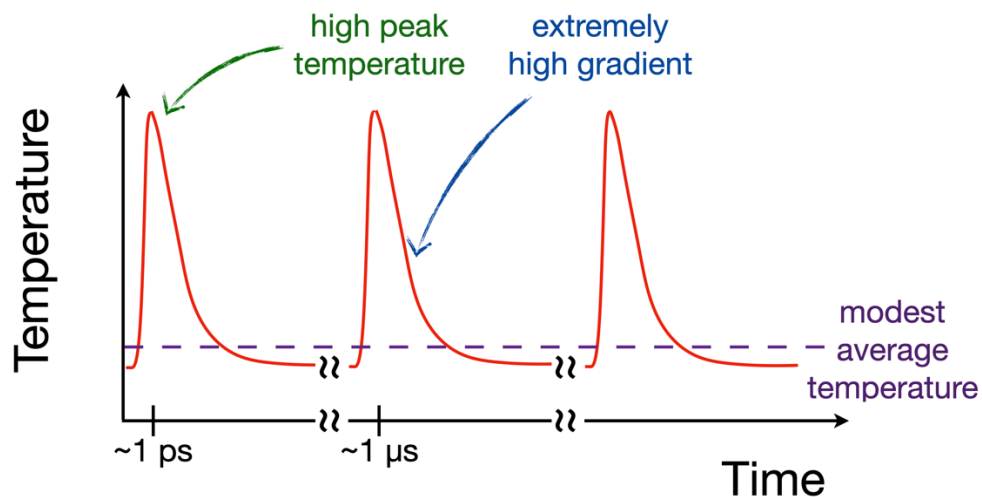


Figure S4. Cartoon-like depiction of local temperature variation under the influence of ultrafast pulse train.

Examples of laser-synthesised zeolites

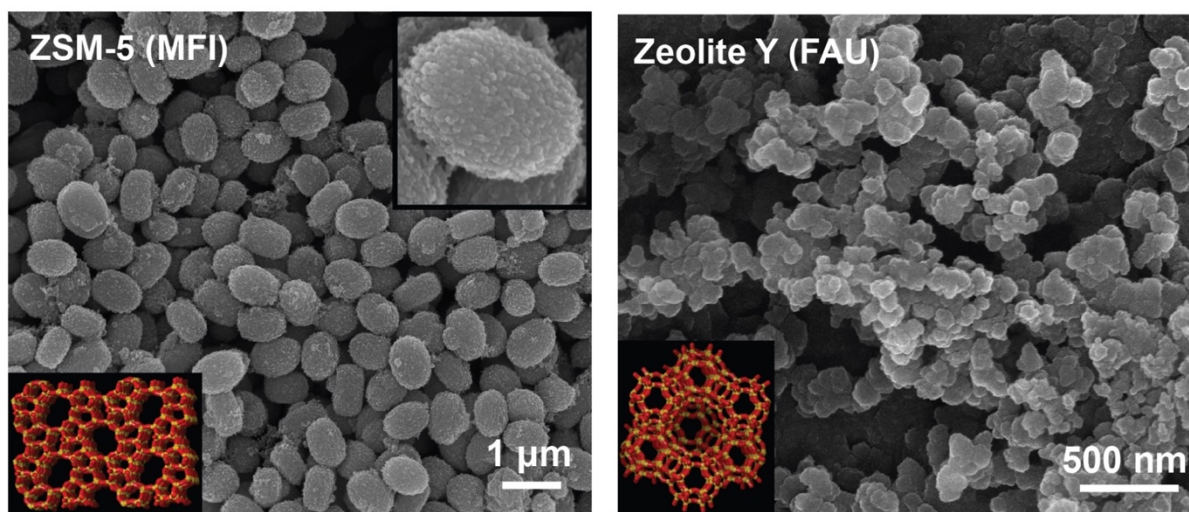


Figure S5. SEM images of (left) microporous ZSM-5 (framework type MFI) and (right) template-free microporous zeolite Y (framework type FAU) synthesised via laser synthesis method.

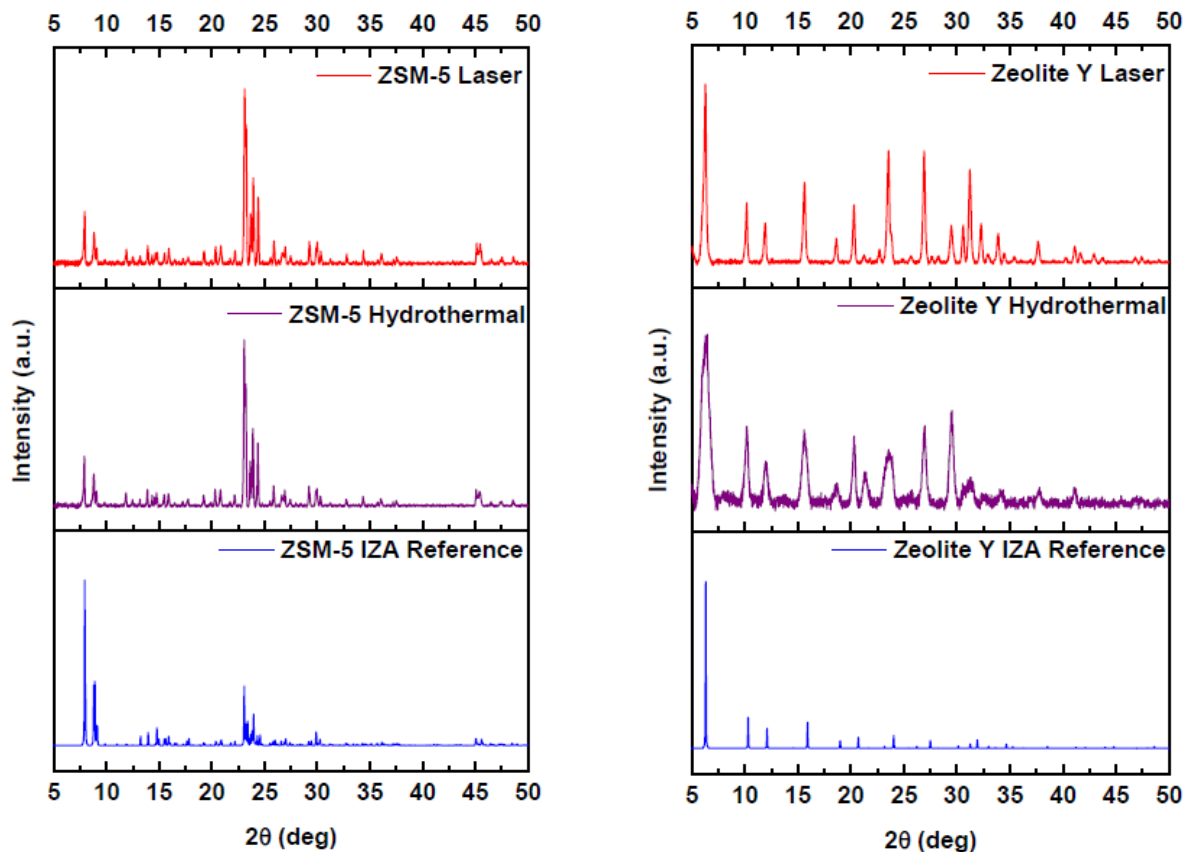


Figure S6. XRD patterns of microporous (left) ZSM-5 and (right) zeolite Y crystals synthesised via laser and hydrothermal synthesis methods. Reference XRD patterns of zeolites are obtained from the International Zeolite Association (IZA)'s webpage.

Repeatability of the laser-synthesised zeolites

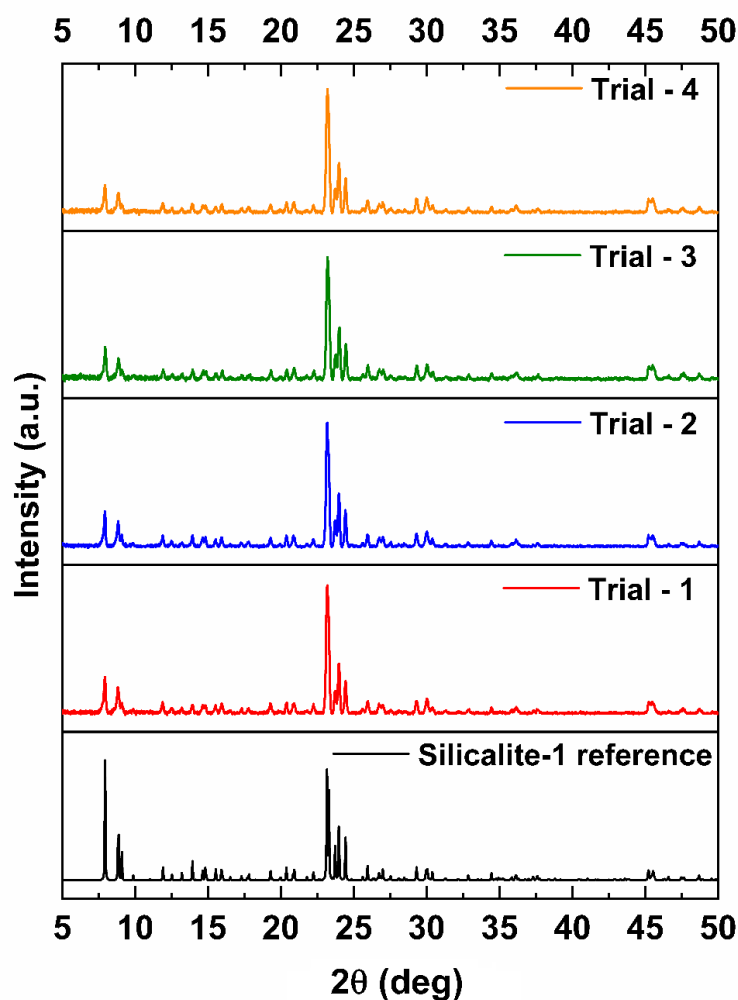


Figure S7. XRD patterns of laser-synthesised TPA-silicalite-1 zeolites, where the original experiment (Trial 1, % crystallinity = 72) was repeated after 2-days (Trial 2, % crystallinity = 86), 1 week (Trial 3, % crystallinity = 75), and 1 month (Trial 4, % crystallinity = 80), and compared to the reference XRD pattern approved by the International Zeolite Association (IZA). % crystallinity is calculated based on the characteristic peaks in 2θ values between 20-25°.

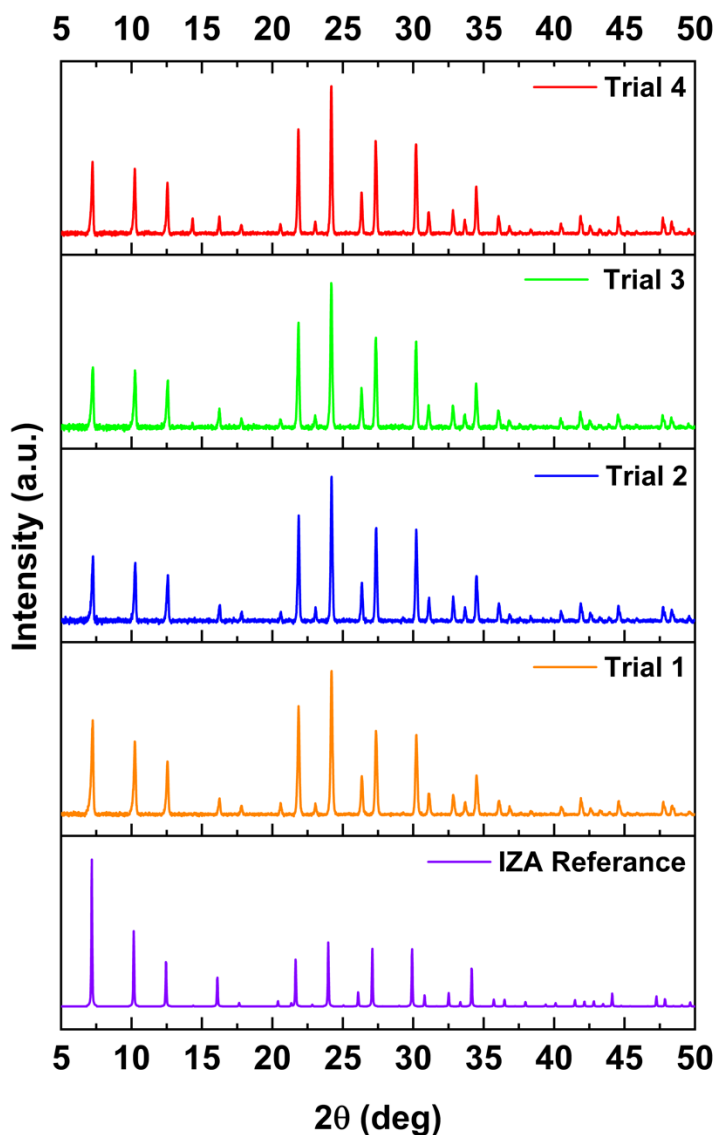


Figure S8. XRD patterns of laser-synthesised Zeolite A, where the original experiment (Trial 1, % crystallinity = 100) was repeated after 1 week (Trial 2, % crystallinity = 96), 1 months (Trial 3, % crystallinity = 95) and 3 months (Trial 4, % crystallinity = 98), and compared to the reference XRD pattern approved by the International Zeolite Association (IZA). The % crystallinity is calculated based on the relative intensity of the 10 most intense characteristic peaks compared to the hydrothermal synthesis of the same synthesis.

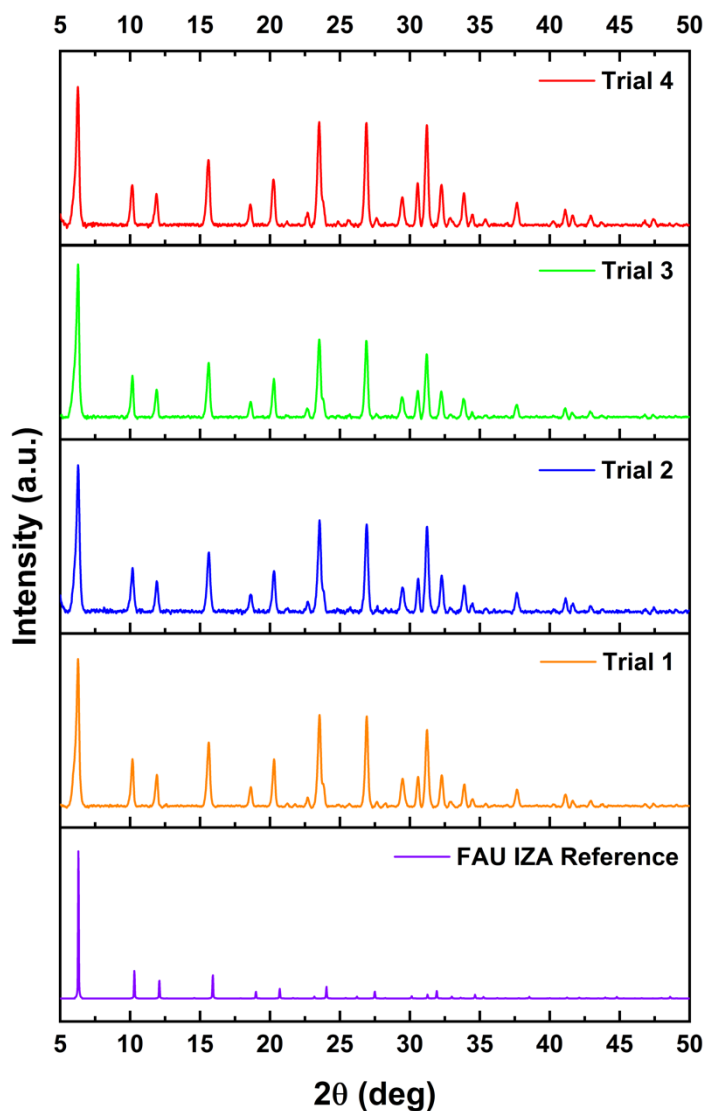


Figure S9. The XRD patterns of laser-synthesized nanosized FAU-type Zeolite Y, where the original experiment (Trial 1, % crystallinity = 96.4) was repeated after 4 months (Trial 2, % crystallinity = 92.1), 7 months (Trial 3, % crystallinity = 87.2), and 8 months (Trial 4, % crystallinity = 100), and compared to the reference XRD pattern approved by the International Zeolite Association (IZA). The % crystallinity is calculated based on the relative intensity of the 5 most intense characteristic peaks compared to most crystalline ultrafast laser Trial 4 since hydrothermally synthesised nanosized FAU has 83.5% crystallinity compared to our most crystalline trial.

Comparison of laser- and hydrothermal-synthesised TPA-Silicalite-1 Zeolites

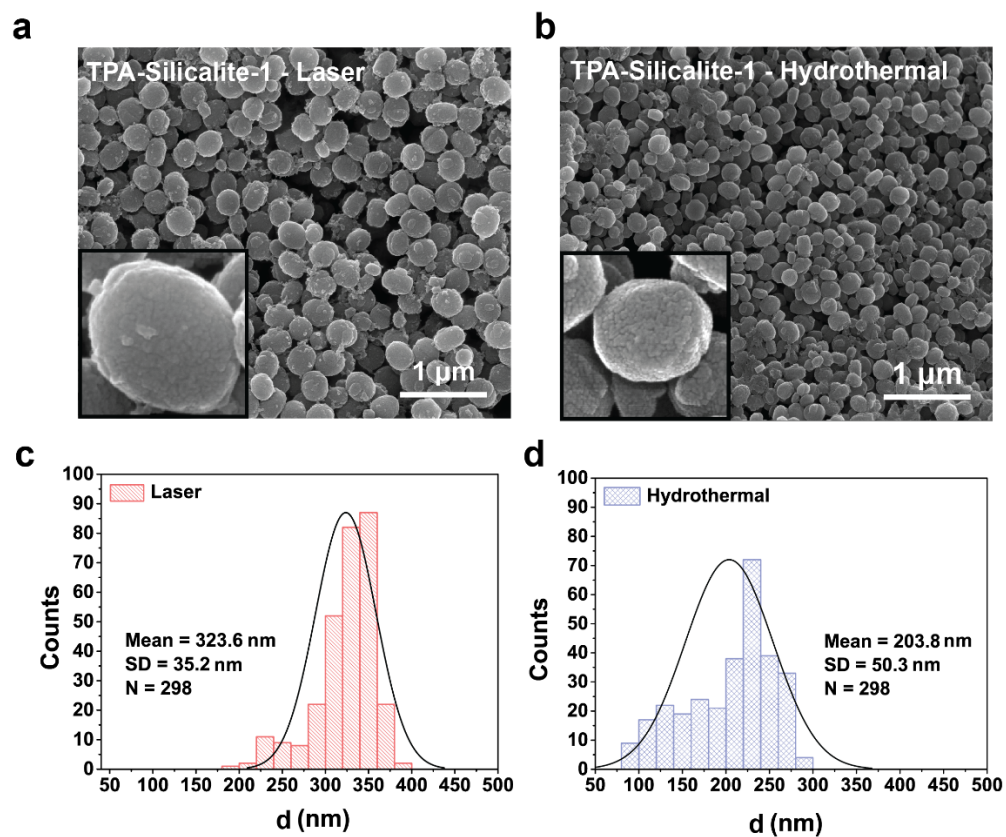


Figure S10. SEM images and the plots show the comparison of the particle size distribution for (a and c) laser- and (b and d) hydrothermal-synthesised zeolites.

Reducing the average crystal size of laser-synthesised TPA-Silicalite-1 Zeolites

In previous hydrothermal synthesis trials where the effect of water content within the precursor suspension was studied, the linear growth rate of zeolite crystals seemed to increase with more water¹. Increasing the water content, all else constant, means a decrease in silica concentration and alkalinity in the synthesis mixture. Alkalinity affects number of particles and their linear growth rate (*i.e.* size). Higher alkalinity induces more number of nuclei to grow. As alkalinity increases (*i.e.*, water content decreases), particles tend to grow slower, resulting in narrower size distribution for hydrothermal and laser synthesis methods.

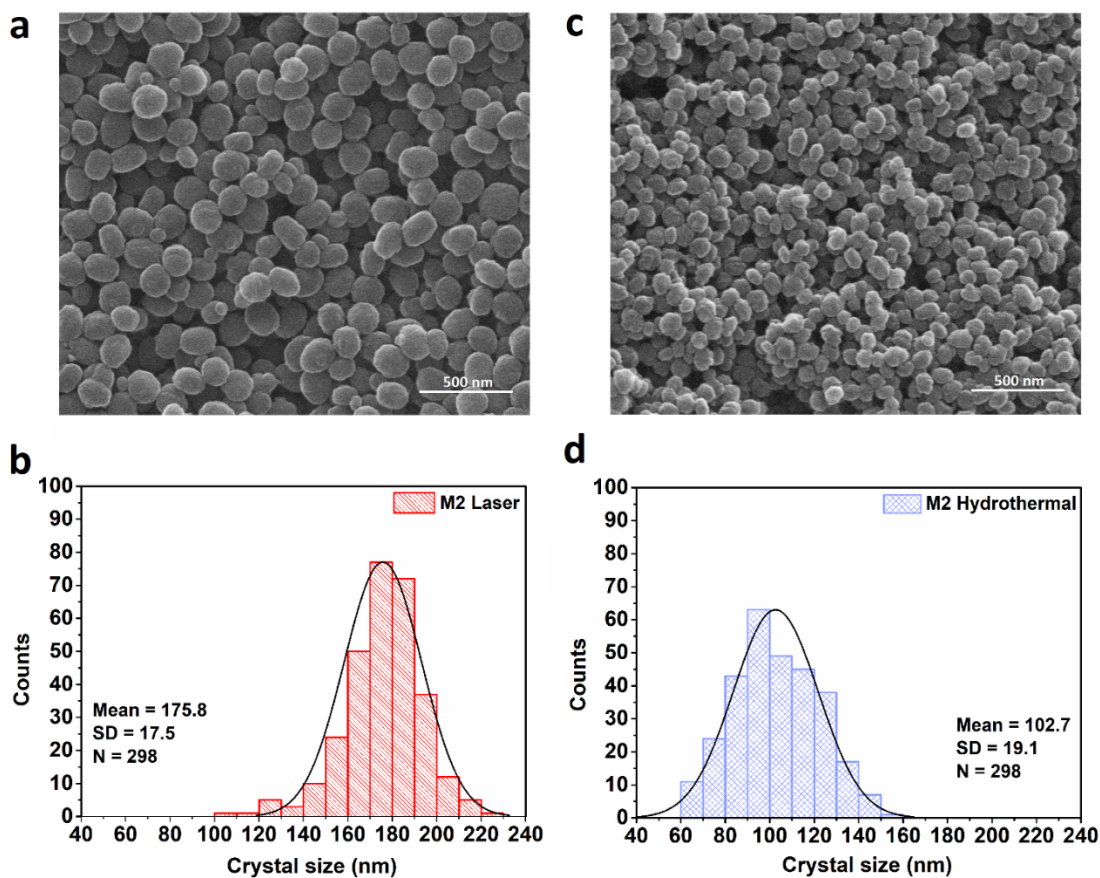


Figure S11. Comparison of (a) laser- and (b) hydrothermal-synthesised TPA – Silicalite-1 crystals using M2 (M2: 25 SiO₂: 9 TPAOH: 480 H₂O: 100 EtOH) molar formula. The rows above and below show SEM images and particle size distributions.

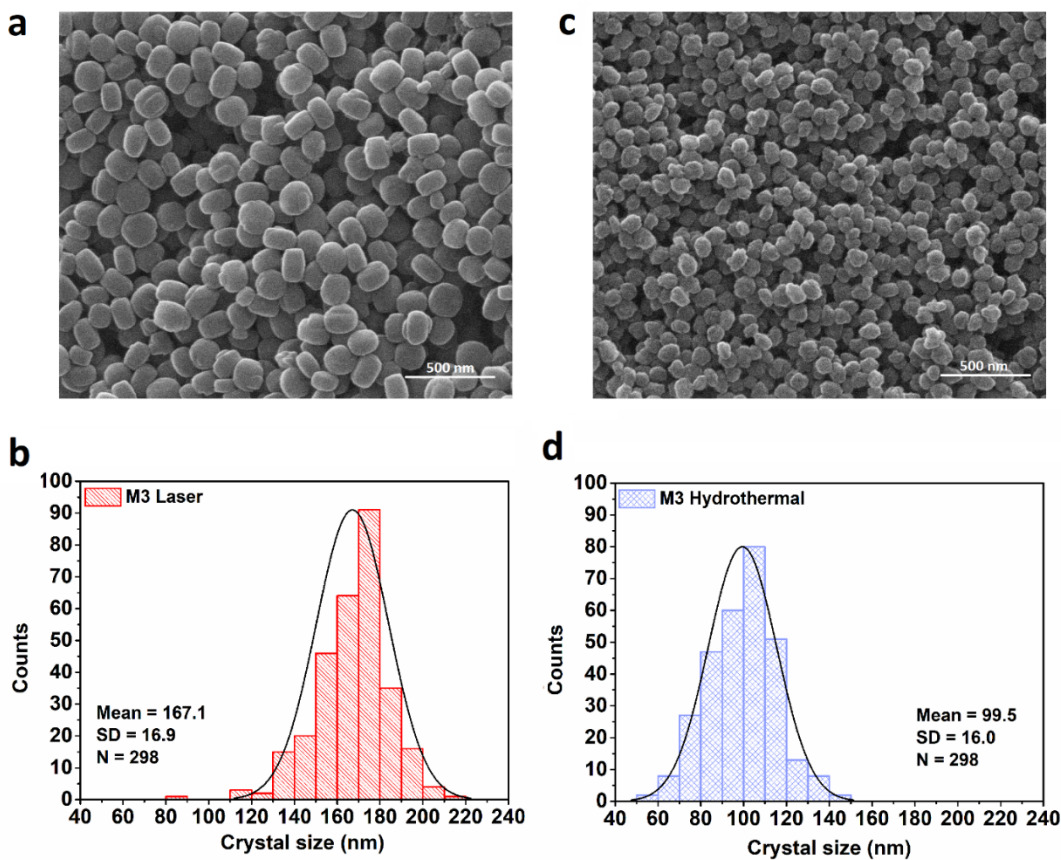


Figure S12. Comparison of (a) laser- and (b) hydrothermal-synthesised TPA – Silicalite-1 crystals using M3 (M3: 25 SiO₂: 9 TPAOH: 450 H₂O: 100 EtOH) molar formula. The rows above and below show SEM images and particle size distributions.

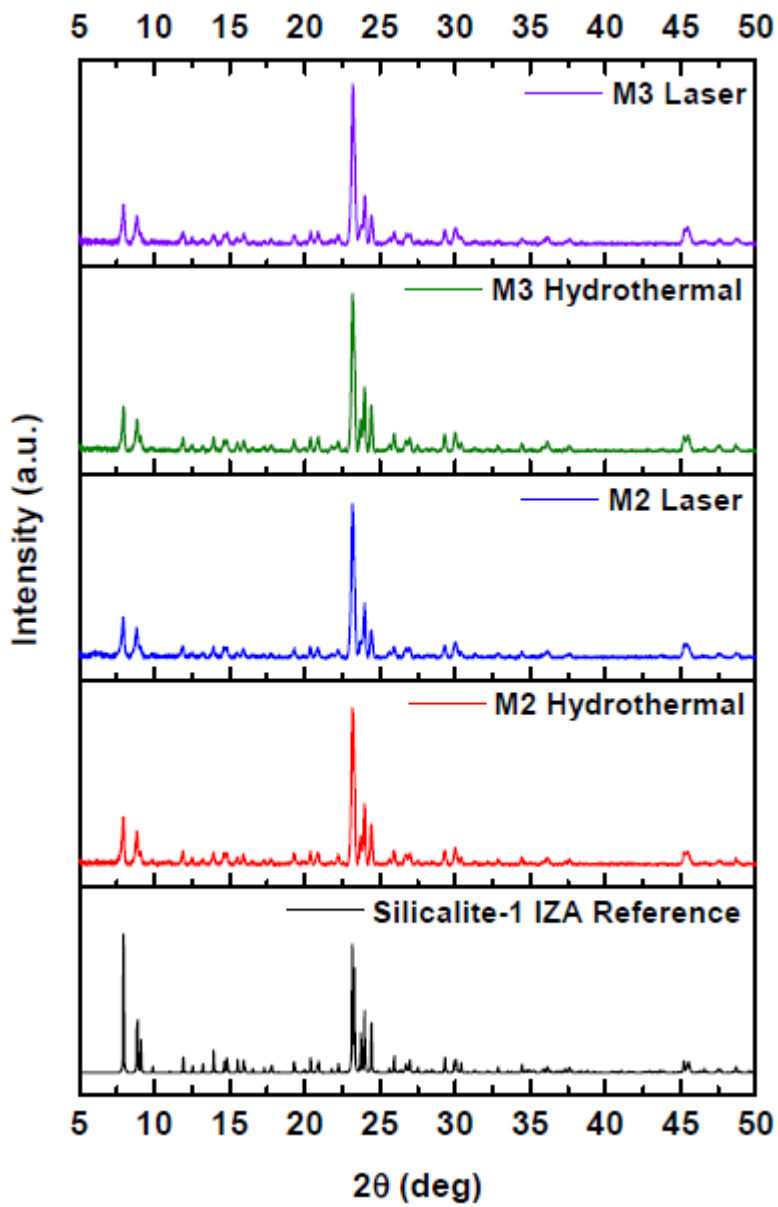


Figure S13. XRD spectrum of laser- and hydrothermal-synthesised TPA-Silicalite-1 zeolites using M2 and M3 molar formulas and compared to the IZA reference.

TGA – Thermal Stability Analysis

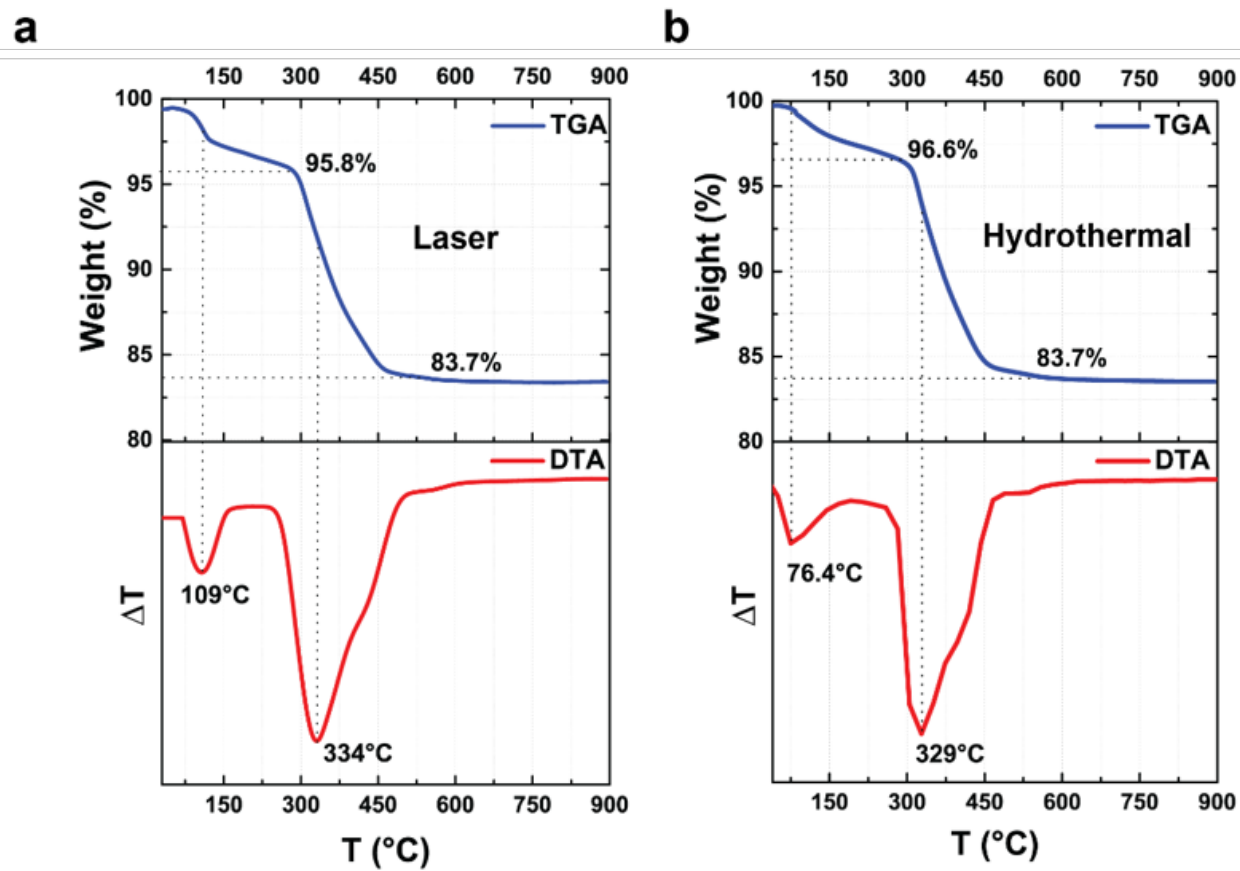


Figure S14. Thermogravimetric (TGA) and Differential Thermal (DTA) curves of TPA-Silicalite-1 synthesised via (a) laser and (b) hydrothermal methods

BET – Porosity and Micropore Volume Analysis

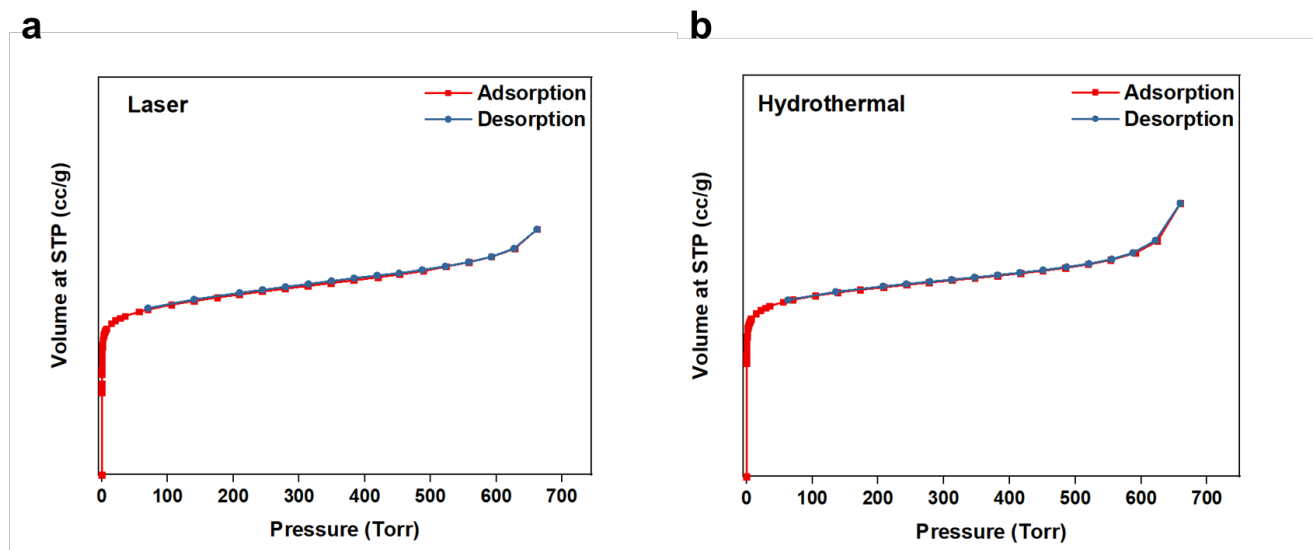


Figure S15. Brunauer-Emmett-Teller (BET) adsorption-desorption isotherms of TPA-Silicalite-1 zeolites (not calcined) synthesised with (a) laser and (b) hydrothermal methods. The BET method facilitated the determination of the total surface area, while the DFT method assessed micropore volume. The BET surface areas were 335.5 m²/g for laser synthesis and 275.0 m²/g for hydrothermal synthesis. The micropore volumes and DFT surface areas were 0.164 cm³/g and 414.8 m²/g for laser synthesis, and 0.130 cm³/g and 299.3 m²/g for hydrothermal synthesis, respectively.

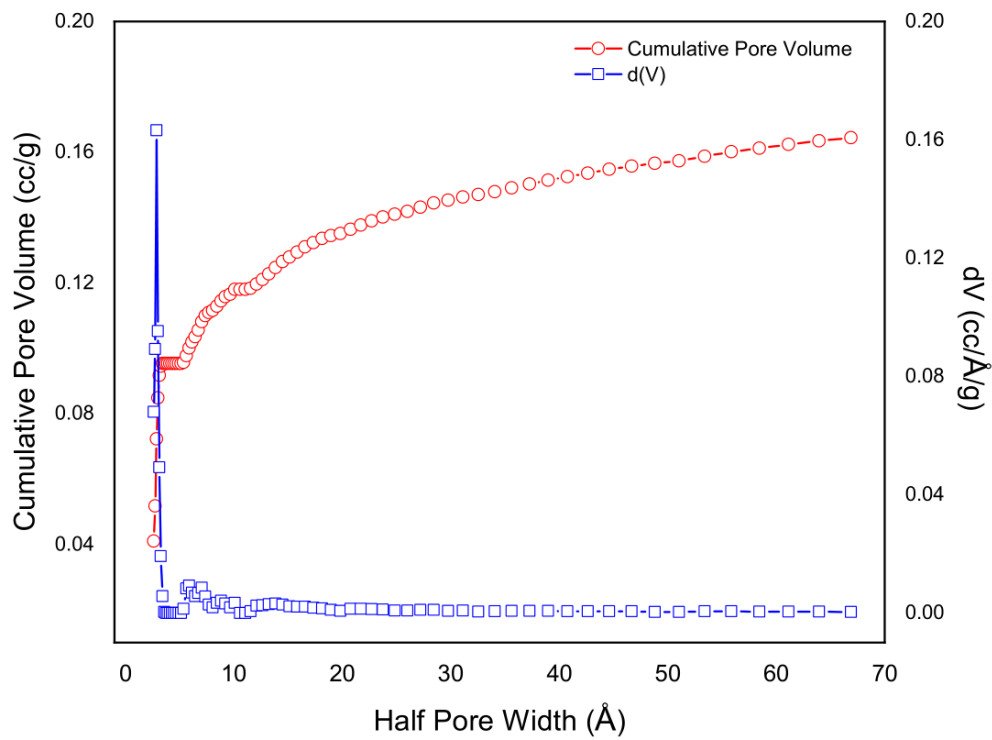


Figure S16. Pore size distribution graph (DFT method) for TPA-Silicalite-1 synthesised via laser method

Peak deconvolution analyses

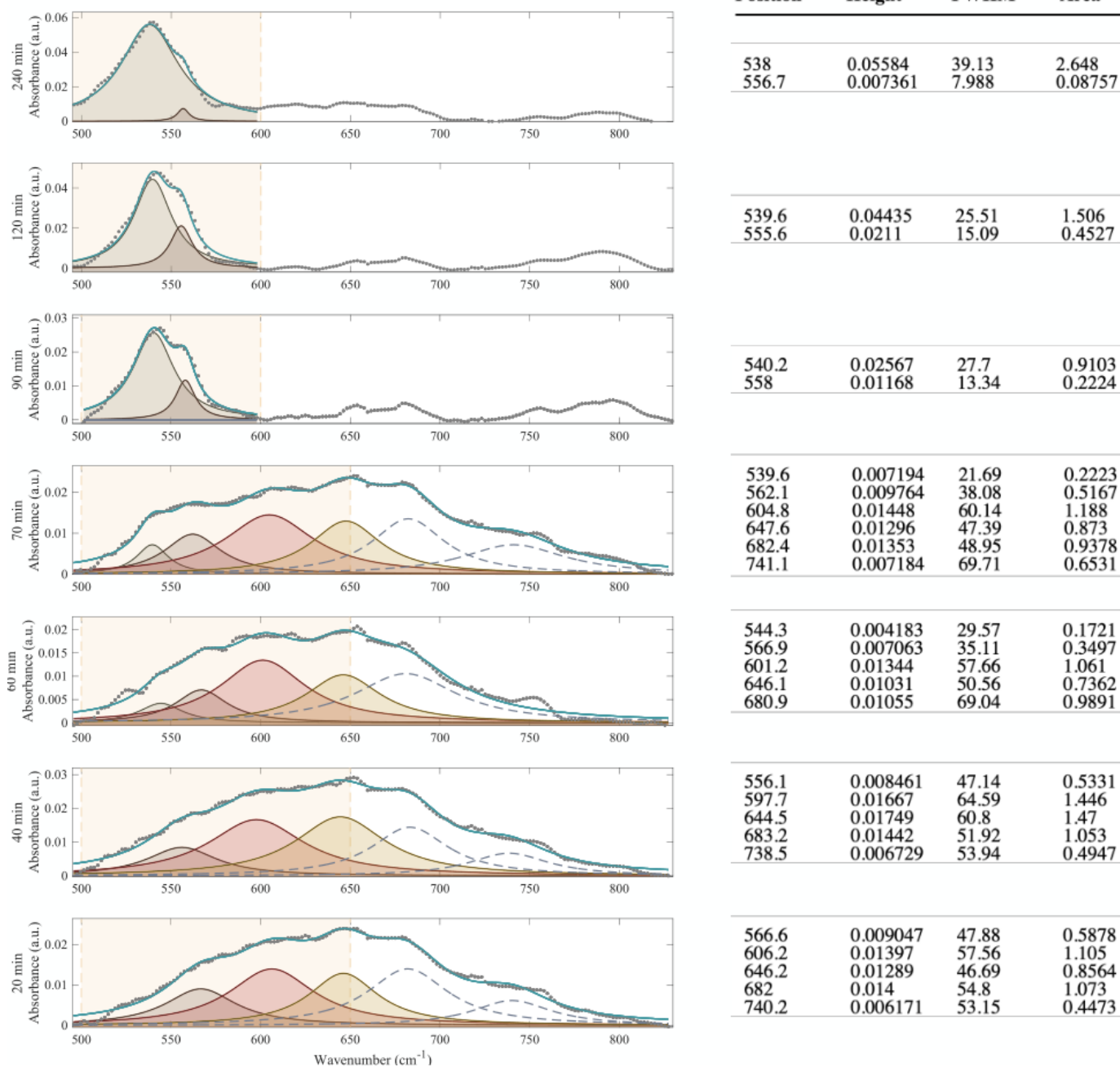


Figure S17. Peak deconvolution of the IR spectrum of zeolites acquired at 20, 40, 60, 70, 90, 120, and 240 minutes of synthesis.

Table S1. Experiments with varying laser parameters and characteristics of the corresponding TPA-Silicalite-1 zeolite samples.

Trial No	Precursor Suspension Volume (μl)	Avg. Power Incident (W)	Avg. Power Absorbed (W)	Pulse Fluence Absorbed (Jcm^{-2})	Pulse Energy Absorbed (μJ)	Synthesis Time (h)	Repetition Rate (kHz)	Total Absorbed Energy ($\text{MJ}/\text{mol}_{\text{SiO}_2}$)	Crystallinity (%)**	Yield (wt. %)
Reference	80	5	1.13	8.84	5.6	3	200	202.5	86	69.7
Trial-1 (T1)*	80	1	0.23	1.77	1.1	15	200	202.5	-	-
Trial-2 (T2)*	80	1.7	0.38	1.77	1.1	9	333	202.5	-	-
Trial-3 (T3)	80	2.5	0.66	1.77	1.1	6	500	202.5	51	55.2
Trial-4 (T4)	80	5	1.13	1.77	1.1	3	1000	202.5	45.3	53.6
Trial-5*	80	2.5	0.56	0.88	0.6	6	1000	202.5	-	-
Trial-6	80	5	1.13	3.54	2.3	3	500	202.5	87	69.7

* Initial transparent colour of the suspension did not change at the end of the reaction. Therefore, powder samples could not be collected for XRD analysis. **The 300-minute saturation sample synthesised with the ultrafast laser method was used as the reference for crystallinity calculations. The differing % crystallinity values for the 3h TPA-Silicalite-1 samples in Table S1 (86%) and Table S3 (78%) result from the fact that Table S3 presents the average crystallinity values of five independent experiments, while Table S1 is based on a single experiment.

Table S2. Crystallinities and yield (wt. %) values of TPA-Silicalite-1 zeolite synthesized via the ultrafast laser method for different reaction times—comparison of TPA - Silicalite-1 crystals synthesized using hydrothermal and femtosecond laser synthesis methods.

	M1		M2		M3	
	Laser	Hydrothermal	Laser	Hydrothermal	Laser	Hydrothermal
Crystallinity (%)	91	100	89	100	81	100
Reaction Time (h)	3	48	3	30	3	30
Yield (wt. %)	69.7	69.2	55.6	59.9	41.7	56.6
Avg. Crystal Size ± SD (nm)	323.6 ± 35.2	203.8 ± 50.4	175.8 ± 17.5	102.7 ± 19.1	167.1 ± 16.9	99.5 ± 16.0
CV (%)	10.9	24.7	10	18.6	10.1	16.1

* M1 = 25 SiO₂: 9 TPAOH: 1450 H₂O: 100 EtOH; M2 = 25 SiO₂: 9 TPAOH: 480 H₂O: 100 EtOH; M3 = 25 SiO₂: 9 TPAOH: 450 H₂O: 100 EtOH. For crystallinity calculations, samples synthesised via the hydrothermal method of each molar formula were taken as reference. The average particle sizes of the crystals were determined from SEM images using Image J software. SD indicates standard deviation. The sample size (N) for particle size distribution analyses was 298. CV indicates Coefficient of Variation (CV = SD/Mean).

Table S3. Crystallinities and yield (wt. %) values of TPA-Silicalite-1 zeolite synthesized via the ultrafast laser method for different reaction times.

Batch Molar Formula	Reaction time (min.)	Color of the suspension	Yield * (wt. %)	Crystallinity (%)*
M1	70	Light Milky	9.3	48
	90	Milky	11.6	55
	120	Opaque white	46.5	62
	150	Opaque white	60.4	69
	180	Opaque white	69.7	78
	200	Opaque white	69.7	88
	220	Opaque white	74.4	96
	240	Opaque white	72.0	99
	260	Opaque white	74.4	98
	280	Opaque white	72.0	99
	300	Opaque white	76.7	100

*The 300-minute saturation sample synthesised with the ultrafast laser method was used as the reference for crystallinity calculations. The differing % crystallinity values for the 3h TPA-Silicalite-1 samples in Table S1 (86%) and Table S3 (78%) result from the fact that Table S3 presents the average crystallinity values of five independent experiments, while Table S1 is based on a single experiment.